

Durham Research Online

Deposited in DRO:

02 June 2020

Version of attached file:

Accepted Version

Peer-review status of attached file:

Peer-reviewed

Citation for published item:

Heap, Michael J. and Gilg, H. Albert and Byrne, Paul K. and Wadsworth, Fabian B. and Reuschlé, Thierry (2020) 'Petrophysical properties, mechanical behaviour, and failure modes of impact melt-bearing breccia (suevite) from the Ries impact crater (Germany).', *Icarus*, 349 . p. 113873.

Further information on publisher's website:

<https://doi.org/10.1016/j.icarus.2020.113873>

Publisher's copyright statement:

© 2020 This manuscript version is made available under the CC-BY-NC-ND 4.0 license
<http://creativecommons.org/licenses/by-nc-nd/4.0/>

Use policy

The full-text may be used and/or reproduced, and given to third parties in any format or medium, without prior permission or charge, for personal research or study, educational, or not-for-profit purposes provided that:

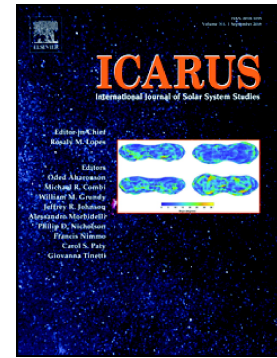
- a full bibliographic reference is made to the original source
- a [link](#) is made to the metadata record in DRO
- the full-text is not changed in any way

The full-text must not be sold in any format or medium without the formal permission of the copyright holders.

Please consult the [full DRO policy](#) for further details.

Petrophysical properties, mechanical behaviour, and failure modes of impact melt-bearing breccia (suevite) from the Ries impact crater (Germany)

Michael J. Heap, H. Albert Gilg, Paul K. Byrne, Fabian B. Wadsworth, Thierry Reuschlé



PII: S0019-1035(20)30253-0

DOI: <https://doi.org/10.1016/j.icarus.2020.113873>

Reference: YICAR 113873

To appear in: *Icarus*

Received date: 11 March 2020

Revised date: 13 May 2020

Accepted date: 22 May 2020

Please cite this article as: M.J. Heap, H.A. Gilg, P.K. Byrne, et al., Petrophysical properties, mechanical behaviour, and failure modes of impact melt-bearing breccia (suevite) from the Ries impact crater (Germany), *Icarus* (2020), <https://doi.org/10.1016/j.icarus.2020.113873>

This is a PDF file of an article that has undergone enhancements after acceptance, such as the addition of a cover page and metadata, and formatting for readability, but it is not yet the definitive version of record. This version will undergo additional copyediting, typesetting and review before it is published in its final form, but we are providing this version to give early visibility of the article. Please note that, during the production process, errors may be discovered which could affect the content, and all legal disclaimers that apply to the journal pertain.

Petrophysical properties, mechanical behaviour, and failure modes of impact melt-bearing breccia (suevite) from the Ries impact crater (Germany)

Michael J. Heap^{1*}, H. Albert Gilg², Paul K. Byrne³, Fabian B. Wadsworth⁴,
Thierry Reuschlé¹

¹*Géophysique Expérimentale, Institut de Physique de Globe de Strasbourg (UMR 7516 CNRS, Université de Strasbourg/EOST), 5 rue René Descartes, 67084 Strasbourg cedex, France.*

²*Lehrstuhl für Ingenieurgeologie, Technische Universität München, Munich, Germany.*

³*Department of Marine, Earth, and Atmospheric Sciences, North Carolina State University, Raleigh, North Carolina, U.S.A.*

⁴*Department of Earth Sciences, Science Labs, Durham University, Durham, DH1 3LE, U.K.*

*Corresponding author: Michael Heap (heap@unistra.fr)

Abstract

The physical properties and mechanical behaviour of impactites are an important parameter in fluid flow models and slope stability and landscape evolution assessments for heavily impacted planetary bodies. We first present porosity, permeability, Young's modulus, and uniaxial compressive strength measurements for

three suevites from the Ries impact crater (Germany). Porosity ranges from 0.18 to 0.43, permeability from 5.8×10^{-16} to $5.1 \times 10^{-14} \text{ m}^2$, Young's modulus from 1.4 to 8.1 GPa, and uniaxial compressive strength from 7.3 to 48.6 MPa. To explore their mechanical behaviour, we performed triaxial deformation experiments on these samples at a range of confining pressures. The brittle–ductile transition for the lowest (0.25) and highest (0.38) porosity suevite samples was at a confining pressure of ~ 30 and ~ 10 MPa, respectively (corresponding to, for example, depths respectively of ~ 1 and ~ 4 km on Mars). Microstructural observations show that the dominant deformation micromechanism during brittle deformation is microcracking, and during ductile deformation is cataclastic pore collapse. We show that a theoretically grounded permeability model for welded granular media accurately captures the permeability of the studied suevites, and we use micromechanical models to glean insight as to their mechanical behaviour. Finally, we upscale our laboratory measurements to provide physical property values for lengthscales more relevant for large-scale models, and we compare these data with those for basalt (a lithology representative of the surface of the inner Solar System bodies). These analyses show how macroscopic fractures serve to increase the permeability and decrease the strength and Young's modulus of suevite; for example, we find that basalt can be a factor of 2–5 stronger than suevite in the shallow crust. Our study suggests, therefore, that the rock masses comprising older, bombarded crusts are substantially weaker and more porous and permeable than the younger plains material on these bodies. These findings should be considered in large-scale fluid flow modelling and when providing crustal strength estimates or slope stability assessments for planetary bodies on which protracted records of impact bombardment are preserved.

Keywords: suevite; porosity; strength; permeability; alteration; Young's modulus

Journal Pre-proof

1 Introduction

Impact craters are a geological feature ubiquitous to the solid-surface planetary bodies of our Solar System (e.g., Neukum et al., 1975; Melosh, 1989; Phillips et al., 1992; Wood et al., 2010; Barnouin et al., 2012; Robbins and Hynek, 2012; Robbins et al., 2017). The preservation of impact craters on Earth is rare, largely due to erosion and tectonic activity (e.g., Grieve and Shoemaker, 1994). However, impact bombardment of bodies in the inner Solar System is all but certain; for example, nearly 400,000 >1 km-diameter craters have been identified on Mars, a few hundred of which are >100 km in diameter (Robbins and Hynek, 2012), and Mercury is similarly marked (e.g., Fassett et al., 2012a). Well-preserved craters on the terrestrial planets and the Moon are associated with impactites, rocks that have either been created or modified by an impact (e.g., Osinski et al., 2011; Stöffler et al., 2018).

On Earth, where we can readily access and assess such deposits (even if they are comparatively rare), proximal impactites have been classified into three groups: shocked target rocks, impact breccias, and impact melt rocks (e.g., Stöffler and Grieve, 2007; Osinski and Pierazzo, 2013; Stöffler et al., 2018). Impact breccias are characterised by their clast contents, the most distinctive of which are impact melt-bearing breccias (“suevites”). Impactites as observed on Earth are also often variably altered (typically argillic alteration and zeolitisation) by the hydrothermal system that forms following the impact (e.g., Osinski et al., 2013; Kirsimäe and Osinski, 2013) or by supergene alteration (Muttik et al., 2010, 2011).

The petrophysical properties of impactites, such as porosity, permeability, Young’s modulus, and strength, are valuable input parameters for a wide range of modelling. For example, the porosity and permeability of impactites are required in models designed to understand fluid flow within the hydrothermal systems associated

with impact craters (e.g., Rathbun and Squyres, 2002; Abramov and Kring, 2004, 2005; Sanford, 2005; Versh et al., 2006; Abramov and Kring, 2007; Barnhart et al., 2010). Further, for heavily impacted crusts such as that of Mars and Mercury, the porosity and permeability of impactites may provide useful constraints for estimates of crustal porosity and permeability. Porosity and permeability estimates of the Martian crust, for example, are required for the modelling of outflow channel formation (e.g., Gulick, 1998; Manga, 2004; Hanna and Phillips, 2005; Andrews-Hanna and Phillips, 2007; Musiol et al., 2011), crustal hydrothermal convection (e.g., Travis et al., 2003), hydrothermal crustal cooling (e.g., Parmentier and Zuber, 2007), methane release into the atmosphere (e.g., Lyons et al., 2005; Etiope et al., 2013), and groundwater flow (e.g., Grimm and Painter, 2009; Harrison and Grimm, 2009). Additionally, knowledge of the mechanical behaviour and strength of impactites is important for our understanding of impact crater collapse (e.g., Melosh and Ivanov, 1999; Wünnemann and Ivanov, 2003), the modelling of impact crater geometry (e.g., Collins, 2004; Potter et al., 2012), and values of uniaxial compressive strength of crustal rocks are needed for characterising the strength and stability of rock masses using tools such as rock mass rating (RMR) or the geological strength index (GSI) (e.g., Schultz, 1993, 2002; Neuffer and Schultz, 2006; Nahm and Schultz, 2007; Okubo et al., 2011; Brunetti et al., 2014; Klimczak, 2015; Klimczak et al., 2015). Further, strength values for impactites could help inform studies that provide rock strength estimates from rover drilling and abrasion data (e.g., Thomson et al., 2013; Peters et al., 2018), as well as improving physical weathering rate estimates (e.g., Viles et al., 2010; Eppes et al., 2015).

Despite the need for robust input parameters for a variety of modelling studies, there are, to our knowledge, only two studies that provide laboratory-measured values

for the permeability of impact melt-bearing breccia (Parnell et al., 2010; Heap et al., 2020a), and but one that provides values of uniaxial compressive strength (Heap et al., 2020a). Other studies have, however, provided other physical property values for impactites. For example, values of density, porosity, thermal conductivity, elastic wave velocities, and magnetic susceptibility are available for impactites from the Chicxulub impact crater (Mexico) (e.g., Mayr et al., 2008a; Elbra and Pesonen, 2011; Christeson et al., 2018). Parnell et al. (2010) found that the permeability of impact breccias from the Haughton (Canada), Ries (Germany), and Rochechouart (France) impact craters to be between $\sim 1 \times 10^{-16}$ and $\sim 1 \times 10^{-15} \text{ m}^2$. Heap et al. (2020a) measured the porosity, permeability, and uniaxial compressive strength of samples of impact melt-bearing breccia collected from two locations at the Ries impact crater. They found average connected porosities of 0.24 and 0.25, and average uniaxial compressive strengths of 34.2 and 29.2 MPa, for samples taken from the quarries at Seelbronn and Altenbürg, respectively. The average permeability of these impact melt-bearing breccias was found to be $\sim 2 \times 10^{-15} \text{ m}^2$ (Heap et al., 2020a). However, notwithstanding these few studies, petrophysical measurements are currently unavailable for altered impactites and thus a full assessment of the mechanical behaviour, failure modes (brittle or ductile), and deformation micromechanisms of impactites is absent. The paucity of studies that report petrophysical and mechanical properties of impactites reflects, in part, the poor preservation potential of impact craters and their impactites on Earth (Grieve and Shoemaker, 1994). As a result, the Ries impact crater (Figure 1), one of only several impact craters on Earth with well-preserved and easily accessible impact melt-bearing breccias (Osinski et al., 2011), serves as an ideal location to sample and study impactites.

The Ries crater (Figure 1) is a double-layer rampart crater with an inner- and outer-ring diameter of about 12 and 24 km, respectively (e.g., Wünnemann et al., 2005; Figure 1), that shares similarities with Martian craters (e.g., Sturm et al., 2013). The crater formed following an impact into a layer of sedimentary rocks 600–700 m thick overlying a crystalline basement (e.g., Pohl et al., 1977; Stöffler et al., 2013) about 15 million years ago (e.g., Rocholl et al., 2018). Types of impactite identified at Ries crater include (von Engelhardt, 1990): shocked target rocks; breccia derived mainly from the sedimentary cover (the “Bunte breccia”, e.g., Hörz et al., 1983); polymict crystalline breccia; impact melt-bearing breccias (“suevite”, e.g., von Engelhardt et al., 1995, 1997); and impact melt rocks (e.g., Osinski, 2004; Pohl et al., 1977). We focus here on providing rock physical and mechanical properties (porosity, permeability, Young’s modulus, compressive strength, and failure mode) for samples of suevite, a type of impact melt-bearing breccia found at the Ries impact crater. There are three types of suevite at Ries crater: (1) “crater suevite”, which is up to 300 m thick and covered by Miocene lake sediments; (2) “outer suevite”, which is only \leq 25 m thick and outcrops up to 22 km from the centre of the structure; and (3) dyke suevite, found in the parautochthonous crater basement and in ejected crystalline megablocks (e.g., Stöffler et al., 2013). These poorly sorted impact melt-bearing breccias formed as a result of the welding of glass/melt and lithic fragments deposited by fluidised granular density currents (e.g., Siegert et al., 2017; see also von Engelhardt, 1997; Newsom et al., 1990; Stöffler et al., 2013) generated following the impact. Suevites at Ries contain centimetre-sized fragments of sedimentary and crystalline rocks (e.g., Graup, 1981; von Engelhardt, 1990, 1997) and angular fragments and aerodynamically shaped bombs of impact melt glass (Stähle, 1972; Osinski, 2003). These clasts are hosted within a matrix of impact melt glass, rock and

mineral fragments, crystallites, and clay minerals (and sometimes zeolites) that formed as a result of post-deposition hydrothermal alteration and weathering (Newsom et al., 1986; von Engelhardt, 1990, 1997; Osinski, 2004, 2005; Muttik et al., 2008, 2011; Sapers et al., 2017). High-pressure minerals, such as coesite (Stöffler, 1966; Stähle et al., 2008) and diamond (Schmitt et al. 2005; Stöffler et al., 2013), have also been identified. Coesite, a high-pressure silica phase, is the mineral that confirmed the impact origin of these deposits in the 1960s (Shoemaker and Chao, 1961).

Here, we present a laboratory study designed to first report the petrophysical properties (porosity, permeability, Young's modulus, and uniaxial compressive strength) of variably altered suevites (impact melt-bearing breccia) from Reis crater (building on data recently published by Heap et al., 2020a). We then present the results of a suite of triaxial deformation experiments designed to better understand and contrast the mechanical behaviour of relatively unaltered and altered suevites. We complement these mechanical data with microstructural work to determine the operative deformation micromechanisms. We then provide permeability and micromechanical modelling to better understand the fluid flow and mechanical properties of these samples. Since upscaled values are of most importance for large-scale models, we use techniques often employed in geotechnical engineering to provide values of strength, Young's modulus, and permeability relevant for longer lengthscales. Finally, we outline the implications of these data for planetary bodies that record protracted periods of impact bombardment.

2 Experimental materials and methods

Blocks of suevite (impact melt-bearing breccia) were collected from three different quarries located within or adjacent to the Ries impact crater in Nördlingen: the Seelbronn quarry (one block: SUE), the Altenbürg quarry (one block: ALT), and the Aumühle quarry (three blocks: AU1, AU2, and AU3) (Figure 1). These blocks were selected due to their visible differences in alteration (colour). The blocks from all three quarries are poorly sorted clastic rocks that contain millimetre- and centimetre-sized clasts of glass (aerodynamically shaped bombs and angular fragments), crystalline rocks (Variscan granites and pre-Variscan gneisses and amphibolites), and sedimentary rocks within a fine-grained matrix (as described in von Engelhardt, 1990, 1997; Stöffler et al., 2013); photographs of representative 25 mm-diameter core samples are shown in Figure 2.

The mineral content of the five blocks was quantified using X-ray powder diffraction (XRPD). Powdered aliquots of each block, containing an internal standard of 20 wt.% ZnO, were ground for 8 min with 10 ml of isopropyl alcohol in a McCrone micronising mill using zirconium dioxide cylinder elements. The XRPD analyses were performed on powder mounts using a Bruker D8 advance eco X-ray diffractometer (CuK α , automatic divergence slit, 15 mm irradiated sample length, anti-air scatter screen, 2.5° primary and secondary soller slits, step-scan from 2 to 75° 2 Θ with 0.01° increments per second, counting time one second per increment, 40 kV, 25 mA). The phases in the whole rock powders were quantified using the Rietveld program BGMN (Bergmann et al., 1998) and Profex 4.0.2 graphical user interface (Döbelin and Kleeberg, 2015). To identify the clay minerals, <2 μ m fractions were also separated by gravitational settling. Oriented mounts containing the <2 μ m fraction were X-rayed in an air-dried and ethylene-glycolated state.

Thin sections were prepared from offcuts taken from blocks from each of the three quarries (SUE, ALT, and AU1) and their microstructure was examined using a Tescan Vega 2 XMU system backscattered scanning electron microscope (SEM).

To assess the pore-throat size distribution of our blocks, we performed mercury injection porosimetry on offcuts (between 3 and 5 g) of blocks SUE, ALT, and AU1 using a Micromeritics Autopore IV 9500. The mercury equilibration time and filling pressure were 10 s and ~3860 Pa, respectively, and the evacuation time and evacuation pressure were 5 min and 50 μmHg , respectively. The pressure range was ~690 Pa to ~414 MPa.

Cylindrical samples were cored from each block in the same orientation with diameters of 20 or 25 mm (Figure 2). These samples were then precision-ground to a nominal length of 40 or 60 mm, respectively. The samples were cored so as to avoid centimetre-sized clasts. The prepared cylindrical samples were then washed with water to remove any water-soluble grinding fluid and vacuum dried at 40 °C in an oven for at least 48 hours.

The connected porosity of each cylindrical sample was then determined using the skeletal (connected) volume of the sample measured by a helium pycnometer (Micromeritics AccuPyc II 1340), and the bulk volume of the sample calculated using the sample dimensions.

Permeabilities of the 25 mm-diameter cylindrical samples were measured with a nitrogen gas permeameter (Farquharson et al., 2016; Heap and Kennedy, 2016) under a confining pressure of 1 MPa. Permeability was measured using the steady-state method. Steady-state volumetric flow rates were determined (using a gas flowmeter) for several differential pressures (acquired with a pressure transducer). These data were used to calculate permeability using Darcy's law and to check

whether the Forchheimer (Forchheimer, 1901) or Klinkenburg (Klinkenburg, 1941) corrections were required. These corrections were applied when necessary on a case-by-case basis.

The 25 mm-diameter samples were deformed uniaxially using a uniaxial load frame. Dry samples were deformed at an axial strain rate of 10^{-5} s^{-1} until macroscopic failure (that is, the formation of a macroscopic fracture). A lubricating wax was placed on the end-faces of the samples to avoid problems with friction between the sample and the pistons. During deformation, axial displacement and axial load were measured with a linear variable differential transducer (LVDT) and a load cell, respectively. The deformation of the loading column itself (including endcaps and piston) was removed from the axial displacement signal. Axial displacement and axial load were converted to axial strain and axial stress using the sample dimensions. The static Young's modulus was calculated using the slope of the strain–stress curve within the linear elastic region (e.g., Heap et al., 2020b).

Triaxial deformation experiments were performed on 20 mm-diameter samples (a detailed schematic of the device is provided in Farquharson et al. (2017)). Dry samples were deformed at a constant strain rate of 10^{-5} s^{-1} until macroscopic failure (for the brittle experiments) or until an axial strain of 6% was reached (for the ductile experiments). A strain of 6% was chosen as a cut-off because this value is large enough for observing the ductile behaviour and for recovering a sample for analysis, but not too large to require unreasonable experimental times. (The choice of this cut-off strain amount does not impact on our interpretation or conclusions.)

Experiments were performed at a range of constant confining pressures, from 2.5 to 80 MPa. Within a given experiment, the confining pressure was held constant using a confining pressure intensifier. Axial displacement and axial load were

measured during deformation using an LVDT and a load cell, respectively. Axial displacement (following removal of the deformation of the loading column) and axial load were converted to axial strain and axial stress, respectively, using the sample dimensions. Additional triaxial experiments were performed in which the differential stress was held at a constant 2 MPa and the confining pressure was increased in steps of 3–15 MPa. The confining pressure was only increased once the axial strain had stabilised, i.e., when the sample had equilibrated to the new confining pressure (with typical durations on the order of 30 minutes to an hour). The confining pressure was increased in this stepwise manner until the onset of inelastic behaviour, signalled by a large increase in axial strain. We assume a simple effective pressure law where the effective pressure (P_{eff}) is the confining pressure minus the pore fluid pressure (zero for the experiments performed herein). We consider compressive stresses and strains as positive.

3 Results

3.1 Mineral content and microstructure

The mineral content for all the blocks collected is provided in Table 1. Blocks SUE and ALT are primarily composed of amorphous phases, plagioclase, smectite, calcite, and quartz, with minor quantities of coesite, K-feldspar, biotite, and Fe oxides, such as hematite or goethite (Table 1). The main difference between blocks SUE and ALT is that SUE contains more plagioclase and ALT contains more calcite (Table 1). The blocks from the Aumühle quarry (AU1, AU2, and AU3), which are all similar in composition, contain much fewer amorphous phases and much more smectite than the blocks from Seelbronn (SUE) and Altenbürg (ALT) (Table 1).

Representative backscattered SEM images of the SUE, ALT, and AU1 blocks are shown in Figure 3. All three blocks contain poorly sorted angular fragments (quartz, calcite, K-feldspar, plagioclase) within a fine-grained matrix (Figure 3). The SEM images clearly show that the block from the Aumühle quarry (AU1; Figure 3c) is much more porous (black pixels) than those from the Seelbronn (SUE; Figure 3a) and Altenbürg (ALT; Figure 3b) quarries. We also note that blocks SUE and ALT are pervasively microcracked (Figures 3a and 3b, respectively).

The pore-throat size distributions for the SUE, ALT, and AU1 blocks are provided as Figure 4. These data show that AU contains a greater volume of large pore throats than SUE and ALT. For example, ~50% of the volume of pore throats within AU are greater than 0.1 μm , whereas pore throats greater than 0.1 μm only comprise 30 and 35% of the volume of pore throats in ALT and SUE, respectively (Figure 4). The ALT sample contains a large volume of small pore throats: ~60% of the volume of pore throats within ALT is less than 0.01 μm , whereas pore throats less than 0.01 μm only comprise 40 and 15% of the volume of pore throats in SUE and AU, respectively.

3.2 Porosity and permeability

The average connected porosities of the blocks from the quarries at Seelbronn (SUE), Altenbürg (ALT), and Aumühle (AU) are 0.238, 0.237, and 0.390, respectively (Table 2). Their average permeabilities are 1.95×10^{-15} , 2.02×10^{-15} , and $8.20 \times 10^{-15} \text{ m}^2$, respectively (Table 2). Our data show that permeability increases as a function of increasing porosity. The samples from Aumühle (AU) are more porous and more permeable than those from Seelbronn (SUE) and Altenbürg (ALT) (Figure 5; Table 2)

3.3 Uniaxial compressive strength and static Young's modulus

Representative axial stress–strain curves for samples from each of the three quarries are provided in Figure 6a. First, axial stress is a non-linearly increasing function of axial strain, typically attributed to the closure of pre-existing microcracks (section “OA” labelled on the SUE curve in Figure 6a). This stage is followed by a quasi-linear elastic stage, from which the static Young's modulus was determined (section “AB”; Figure 6a). Following the elastic deformation stage, the axial stress is a non-linearly decreasing function of axial strain, typically interpreted as due to the nucleation and growth of microcracks (section “BC”; Figure 6a). The peak stress (the uniaxial compressive strength of the sample) is followed by strain softening and a stress drop associated with the macroscopic failure of the sample (Figure 6a). The average uniaxial compressive strengths of the blocks from the quarries at Seelbronn (SUE), Altenbürg (ALT), and Aumühle (AU) are 34.2, 29.2, and 12.9 MPa, respectively (Table 2). Our data show that uniaxial compressive strength decreases as a function of increasing porosity. The samples from Aumühle (AU) are weaker than those from Seelbronn (SUE) and Altenbürg (ALT) (Figure 6; Table 2).

Static Young's modulus as a function of connected porosity is shown in Figure 7. The average Young's moduli are 6.5, 5.7, and 3.0 GPa for the blocks from the quarries at Seelbronn (SUE), Altenbürg (ALT), and Aumühle (AU), respectively (Table 2). We find that Young's modulus decreases as a function of increasing porosity. The samples from Aumühle (AU) have a lower Young's modulus than those from Seelbronn (SUE) and Altenbürg (ALT) (Figure 7; Table 2)

3.4 Triaxial deformation experiments

The stress–strain curves for the triaxial deformation experiments are shown in Figures 8a (for SUE) and Figure 8b (for AU1) (a mechanical summary of the triaxial experiments performed for this study is provided in Table 3). The suevites from Seelbronn and Aumühle were selected for triaxial testing because they represent the endmembers in terms of alteration, porosity, and strength (Table 2). For sample SUE, the experiments performed at P_{eff} of 0, 5, 10, and 15 MPa clearly show the post-peak stress drop associated with brittle behaviour (i.e., the formation of a shear fracture; see Wong and Baud (2012) for a review on brittle and ductile behaviour of porous rocks). The differential stress at failure also increases as the effective pressure increases from 0 to 15 MPa (Figure 8a; Table 3). Although the stress–strain curve for the sample deformed at 20 MPa appears to be different to those for samples deformed at pressures ≤ 15 MPa, there is a subtle stress drop (following an axial strain of $\sim 5\%$; Figure 8a). The sample deformed at 20 MPa can therefore be considered brittle (the post-deformation sample contained a shear fracture), but its style of failure is very close to the transition between brittle and ductile behaviour.

The stress–strain curves for the samples deformed at 30, 50, and 80 MPa are typical of ductile behaviour: there is no peak stress or stress drop associated with the formation of a shear fracture (Figure 8a; Wong and Baud, 2012). Further, the experiments performed at 50 and 80 MPa show strain-hardening behaviour (where differential stress increases as a function of axial strain: Figure 8a). For sample AU1, the experiments performed at P_{eff} of 0, 2.5, and 5 MPa deformed in a brittle manner, whereas the experiments performed at P_{eff} of 10, 15, and 20 MPa were ductile (Figure 8b). The tests performed at P_{eff} of 15 and 20 MPa show strain-hardening behaviour (Figure 8b). The block from the quarry at Aumühle (AU1) therefore transitioned from

brittle to ductile behaviour at a lower effective pressure (i.e., depth) than the block from Seelbronn (SUE).

3.5 Post-deformation microstructures

To better understand the operative micromechanical processes during brittle and ductile behaviour, thin sections were prepared of the samples of SUE deformed at P_{eff} of 10 and 80 MPa. Backscattered SEM images of the sample deformed at 10 MPa (i.e., in the brittle regime) show a large shear fracture and associated off-fault microcracking (orientated sub-parallel to the maximum principal stress) (Figures 9a and 9b). The sample deformed at 80 MPa (i.e., in the ductile regime) did not contain a shear fracture. Instead, deformation was accommodated by the cataclastic collapse of pores (Figures 9c and 9d). Microcracks are seen to radiate from the collapsed pores (Figure 9c and 9d).

4 Discussion

4.1 The permeability of impact melt-bearing breccia

Although data in the literature are rare, the permeability of the suevites measured herein (Table 2) compare well with published measurements. For example, Parnell et al. (2010) determined the permeability of two samples from the Ries crater to be 1.58×10^{-15} and $2.67 \times 10^{-15} \text{ m}^2$. These authors also reported the permeability of samples from the impact craters at Rochechouart and Haughton as $\sim 1 \times 10^{-15} \text{ m}^2$ and between $\sim 1 \times 10^{-16}$ and $\sim 1 \times 10^{-15} \text{ m}^2$, respectively. The permeability of impact melt-bearing breccia from the Chicxulub impact crater was estimated as between $\sim 1 \times 10^{-18}$ and $\sim 1 \times 10^{-15} \text{ m}^2$ (Mayr et al., 2008b). These measurements highlight a remarkable

similarity worldwide in permeability of impact melt-bearing breccia from different impact craters formed within different lithologies. In strong contrast, the permeability of lavas of the same composition, erupted from the same volcano, can vary by as much as five or six orders of magnitude (e.g., Farquharson et al., 2015).

We compare our suite of data with a model for the permeability of partially welded granular media (Wadsworth et al., 2016) that has been validated against geological porous materials including welded volcanic rocks and sandstones of various diagenetic maturity. This model starts from the assumption that the system was first a granular deposit of particles with mean radius $\langle r \rangle$. Because suevite-forming systems begin as droplets and particles deposited in density currents, this is a valid starting assumption, and consistent with similar cases such as the permeability of variably welded deposits of pyroclastic density currents. From that initial granular state, the model assumes that the particles weld together, reducing the internal pore surface areas. Typically, the Wadsworth et al. (2016) model would require a solution to relate the particle size distribution centred around $\langle r \rangle$ to a distribution of sizes of characteristic pores centred around $\langle a \rangle$. However, here we have directly measured $\langle a \rangle$ (Figure 4), negating the need for this interim step.

We take the $\langle a \rangle$ from the SUE measurement of pore-throat sizes (Figure 4) as intermediate among the three measurements, and find that $\langle a \rangle = 1.09 \mu\text{m}$ (we therefore assume that the pore-throat size is a good approximation of the pore size). We then assume that the pore surface area, s , is related by (Torquato, 2013):

$$s = - \frac{3(1 - \phi) \ln(1 - \phi)}{\langle a \rangle} \quad (1).$$

This relation assumes that s is given by the surface area of a suite of overlapping spherical pores (Wadsworth et al., 2016). The permeability, k , is given by (Wadsworth et al., 2016; Martys et al., 1994):

$$k = \frac{2[1 - (\phi - \phi_c)]}{s^2} (\phi - \phi_c)^n \quad (2),$$

where ϕ_c is the percolation threshold below which all the pores have pinched off, and the permeability is zero, and n is a percolation exponent. On theoretical grounds, $n = 4.4$ was derived for porous overlapping sphere systems (Halperin et al., 1985), leaving only ϕ_c unconstrained in this model.

We fit Equation (2) to our complete dataset, allowing ϕ_c to vary freely using a root-mean-square error between model and data as a minimisation target. We find that the best results are found using $\phi_c = 0.075$ and that to within 5% accuracy, $0.06 \lesssim \phi_c \lesssim 0.1$ is valid. This range of values is consistent with the range of ϕ_c found for sintering or welding angular particles (Wadsworth et al., 2016; Heap et al. 2019). Therefore, what we present is a theoretically grounded model for the permeability of welded granular media that is applicable to suevites across the range of porosities measured herein (Figure 10).

4.2 The uniaxial compressive strength and Young's modulus of impact melt-bearing breccia

To our knowledge, the values of uniaxial compressive strength for suevites reported here (Table 2) and in Heap et al. (2020a) are the only such values yet reported for this rock type. Nonetheless, we find that the samples we assay here have properties similar to other rock types found on Earth. For example, poorly sorted

clastic volcanic rocks from Mt. Meager volcano, Canada—welded block-and-ash flow deposits—have a similar strength to the samples we report here. The uniaxial compressive strength of welded block-and-ash flow from Mt. Meager volcano is ~20 MPa when the porosity is between 0.2 and 0.25 (i.e., the porosity range of the samples measured herein: Table 2) (Heap et al., 2015a); this strength value lies between those we find for the Altenbürg (ALT) and Aumühle (AU) samples (Figure 6b).

Our data show that uniaxial compressive strength decreases as a function of increasing porosity (Figure 6b), in agreement with studies on sedimentary (e.g., Chang et al., 2006; Baud et al., 2014) and volcanic rocks (e.g., Al-Harthi et al., 1999; Heap et al., 2014a; Schaefer et al., 2015; Harnett et al., 2019). Although the relatively high porosity of the samples from Aumühle quarry could explain their relative weakness, we also note that studies have shown that alteration can result in a strength reduction (e.g., del Potro and Hürlimann, 2009; Pola et al., 2012; Wyering et al., 2014; Frolova et al., 2014). The blocks from the Aumühle quarry are more altered than those from Seelbronn or Altenbürg: more of the amorphous phases have been altered to smectite (Table 1). Therefore, the relative weakness of samples from Aumühle (Figure 6b) can be explained by a combination of their higher porosity and greater degree of alteration.

The pore-emanating crack model of Sammis and Ashby (1986) is often used to better understand the mechanical behaviour of porous materials, including rocks (e.g., Baud et al., 2014). This model describes a two-dimensional elastic medium populated by circular pores of uniform radius r . Tensile cracks emanate (in the direction of the maximum principal compressive stress) when the applied stress reaches the critical stress intensity factor, K_{IC} (sometimes called the fracture toughness). These cracks then propagate and coalesce to induce the macroscopic

failure of the elastic medium. An analytical approximation of the pore-emanating crack model of Sammis and Ashby (1986) was derived by Zhu et al. (2010) in the case of uniaxial compression, to model the uniaxial compressive strength, σ_p , as a function of porosity, ϕ :

$$\sigma_p = \frac{1.325}{\phi^{0.414}} \frac{K_{IC}}{\sqrt{\pi r}} \quad (3).$$

The two unknowns in the equation are K_{IC} and r . Therefore, at this stage, it is prudent to first estimate the value or values of the term $K_{IC}/\sqrt{\pi r}$ that best describe the experimental data. Our experimental data cannot be well described using a single value of $K_{IC}/\sqrt{\pi r}$ (Figure 11). The data can be bracketed between two theoretical curves where $K_{IC}/\sqrt{\pi r}$ equals 3.5 and 20 MPa (Figure 11). In the absence of measurements of K_{IC} for impact melt-bearing breccia, we can use the value of K_{IC} identified to describe the welded block-and-ash flow deposits from Mt. Meager volcano: $K_{IC} = 0.15 \text{ MPa.m}^{-1/2}$ (Heap et al., 2015a). This value of K_{IC} yields values of r between ~ 18 and $\sim 585 \text{ }\mu\text{m}$. Therefore, if $K_{IC} = 0.15 \text{ MPa.m}^{-1/2}$ is an appropriate value, our modelling suggests that strength of the suevites is controlled by the largest pores (see our microstructural analysis and our mercury injection data; Figures 3 and 4). Of note, the pore-emanating crack model of Sammis and Ashby (1986) describes a medium that contains pores of a uniform radius, which we know to be a simplification of our experimental materials (see Figures 3 and 4). We further emphasise that the K_{IC} of the block from Aumühle may be lower than that for the other blocks due to the greater alteration intensity (Table 1). Finally, the blocks from Seelbronn and Altenbürg also contain microcracks, which are not considered in the Sammis and

Ashby (1986) model. Nevertheless, micromechanical models such as that proposed by Sammis and Ashby (1986) can help glean information as to the first-order controls on the mechanical behaviour and strength of brittle materials.

To our knowledge, the values of Young's modulus for suevites reported here (Table 2) are the only such values reported. Our data show that Young's modulus decreases as a function of increasing porosity (Figure 7), in agreement with previous studies (e.g., Heap et al., 2020b). Chemical alteration is also known to influence the Young's modulus of rocks and can result in increases to Young's modulus when the alteration is pore-filling (e.g., Frolova et al., 2014; Mordensky et al., 2018; Durán et al., 2019) and decreases to Young's modulus in the case of dissolution (e.g., Frolova et al., 2014). The low Young's modulus of samples from Aumühle (Figure 7) can therefore be explained by a combination of their higher porosity and greater degree of alteration.

4.3 Failure envelopes for impact melt-bearing breccia

The mechanical behaviour of porous materials is best compared on a graph of differential stress, Q , as a function of the effective mean stress, P (Wong and Baud, 2012). P is given by $P = (\sigma_1 + 2\sigma_3)/3 - Pp$, where Pp is the pore fluid pressure (0 MPa in our experiments), σ_1 is the maximum principal compressive stress (the axial stress in our experiments), and σ_3 is the minimum principal compressive stress (the confining pressure in our experiments). The failure envelope of a material can be delineated by plotting the differential stress at failure as a function of the effective mean stress at failure. Deformation experiments must therefore be performed at a range of effective pressures to map the failure envelope.

Failure in the brittle regime is defined as the differential stress at the peak stress (as indicated in Figure 6a), and failure in the ductile regime is defined as the differential stress at the onset of inelastic compaction, termed C^* (Wong and Baud, 2012). P^* is the term given for the onset of inelastic compaction under hydrostatic conditions (i.e., when $Q = 0$) (e.g., Zhang et al., 1990; Wong and Baud, 2012). C^* was determined using the evolution of the volume of the sample during deformation, monitored by the confining pressure intensifier. C^* can be observed as an inflection point in the data of differential stress as a function of the change in confining fluid volume (i.e., sample volume).

In our experiments in which we held the differential stress at 2 MPa and increased the confining pressure, C^* was 2 MPa and P was calculated using the confining pressure required for inelastic compaction (monitored using the axial strain signal). A sample can be considered pre-failure if the state of stress plots inside the failure envelope, and failed if the state of stress plots outside the failure envelope. The sample will have failed in a brittle or ductile manner if the stress state falls outside the failure envelope to the left or right, respectively. The failure envelopes for the suevites from Seelbronn (SUE) and Aumühle (AU1) are shown in Figure 12 (with data available in Table 3). The failure envelope for SUE is much larger than that for AU1. In other words, SUE is pre-failure for much more of the stress space represented. The transition from brittle to ductile behaviour, represented by the “top” of the failure envelope, is at an effective pressure of ~30 and ~10 MPa for SUE and AU1, respectively (Table 3). As discussed above, the relative weakness of the blocks from Aumühle is likely due to a combination of higher porosity (Tables 2 and 3) and greater alteration intensity (Table 1) than for the samples from Seelbronn or

Altenburg. The position of P^* for SUE and AU1 is estimated to be 90 ± 5 and 22 ± 5 MPa, respectively (Figure 12).

4.4 Deformation micromechanisms

Our microstructural work indicates that the operative deformation micromechanisms of these suevite samples are microcracking and cataclastic pore collapse in the brittle and ductile fields, respectively (Figure 9a and 9b). Failure in the brittle regime is the result of the initiation and propagation of microcracks, preferentially aligned to the direction of maximum principal compressive stress (Figure 9a and 9b), which coalesce to form a macroscopic, through-going shear fracture (see also Lockner et al., 1991; Aben et al., 2019). Porosity reduction in the ductile regime is driven by the cataclastic collapse of pores (Figure 9c and 9d). This deformation micromechanism has been previously observed in porous limestones (e.g., Zhu et al., 2010; Vajdova et al., 2012) and porous volcanic rocks (e.g., Loaiza et al., 2012; Adelinet et al., 2013; Zhu et al., 2011; Heap et al., 2015b, 2015c; Zhu et al., 2016).

Of particular interest, because of their ability to reduce permeability and create permeability anisotropy, is whether such compaction is localised into bands. Compaction bands have been well documented in studies on porous sandstone, and form as a result of grain crushing (e.g., Baud et al., 2004, 2006; Fortin et al., 2006; Stanchits et al., 2009; Baud et al., 2015). Compaction bands have also been observed in porous limestones (e.g., Cilona et al., 2014; Baud et al., 2017; Huang et al., 2019) and porous volcanic rocks (e.g., Loaiza et al., 2012; Adelinet et al., 2013; Heap et al., 2015b, 2017a). We observed no evidence of compaction bands in our samples: pore collapse (Figure 9c and 9d) was distributed throughout the sample. In addition, we did

not observe small stress drops in the ductile stress–strain curves (Figure 8), which have also been associated with the formation of compaction bands in laboratory experiments. Therefore, similar to porous tuff from Alban Hills, Italy (Zhu et al., 2010) and Whakaari volcano, New Zealand (Heap et al., 2015c), i.e., granular volcanic rocks with a similar genesis and texture to the suevites studied herein, inelastic compaction in suevite does not appear to localise into bands. The absence of compaction bands in these materials may be related to their wide grain size distribution (e.g., Figure 3), a factor known to suppress compaction localisation in sandstones (Cheung et al., 2012).

4.5 Micromechanics of hydrostatic compaction

To investigate the micromechanics of hydrostatic compaction, we follow the approach outlined by Zhu et al. (2011). By considering the stresses required to yield a single macropore embedded within an effective medium, and by adopting the Mohr–Coulomb failure criterion, the onset of inelastic hydrostatic compaction, P^* , is related to uniaxial compressive strength by (Zhu et al., 2011):

$$P^* = 2\sigma_p/3 \quad (4).$$

Figure 13a shows P^* as a function of uniaxial compressive strength for the SUE and AU1 suevites and a collection of tuffs (volcanic rocks that share textural similarities to the studied suevites). All of these data plot above the theoretical line delineated by Equation (4). As discussed in Zhu et al. (2011), this distribution of samples is likely because the effective medium is less porous than the matrix of these rocks, i.e., the matrix contains numerous micropores, as exposed by our microstructural observations

(Figure 3) and our mercury injection experiments (Figure 4). We can study the influence of micropores on the onset of inelastic hydrostatic compaction by combining Equations (3) and (4) (Zhu et al., 2011):

$$S^* = \frac{K_{IC}}{(\phi_*/\phi)^{0.414} \sqrt{\pi a^*}} \quad (5),$$

where a^* is the average radius of a micropore, ϕ_* is the porosity of the effective medium, and S^* captures the cooperative influence of the fracture toughness, micropore radius, and the partitioning of macro- and microporosity (Zhu et al., 2011). This model describes a dual porosity medium of a macropore surrounded by many micropores. We find that SUE and AU1 are best described by values of S^* of 70 and 14 MPa, respectively (Figure 13b). We note that these values of S^* are similar to those predicted for tuffs (Figure 13b; Zhu et al., 2011).

The average micropore radius can then be estimated using $a^* > (K_{IC}/S^*)^2/\pi$ (Zhu et al., 2011). Assuming $K_{IC} = 0.15 \text{ MPa}\cdot\text{m}^{-1/2}$ (Heap et al., 2015a), the average micropore radius for SUE and AU1 are 1.5 and 36.5 μm , respectively. These pore radii predictions are in agreement with the pore throat radii determined by our mercury injection experiments (Figure 4). The modelling described above therefore highlights an important role for micropores in controlling the onset of inelastic hydrostatic compaction in the studied materials.

4.6 Upscaling laboratory measurements for use in large-scale modelling

The laboratory experiments described herein were performed on samples with diameters of 20 or 25 mm. These measurements, therefore, do not consider the influence of macroscopic fractures, which are well known to influence permeability

(e.g., Brace, 1984; Clauser, 1992; Neuman, 1994; Heap and Kennedy, 2016; Farquharson and Wadsworth, 2018), strength (e.g., Hoek et al., 2002), and Young's modulus (e.g., Hoek and Diederichs, 2006). Since the crusts of heavily impacted planetary bodies are likely highly fractured (e.g., Wieczorek et al., 2013; Heap et al., 2017b; Lognonné et al., 2020), these laboratory values must be upscaled before they can be used in large-scale models.

The strength of a fractured rock-mass can be estimated with the generalised Hoek–Brown failure criterion (Hoek et al., 2002):

$$\sigma'_1 = \sigma'_3 + C_o \left(m_b \frac{\sigma'_3}{C_o} + s \right)^a \quad (6),$$

where σ'_1 and σ'_3 are the effective maximum and minimum principal stresses, respectively, C_o is the laboratory-measured uniaxial compressive strength, and m_b , s , and a are unitless fitting parameters (Hoek et al., 2002):

$$m_b = m_i \exp\left(\frac{GSI - 100}{28 - 14D}\right) \quad (7),$$

$$s = \exp\left(\frac{GSI - 100}{9 - 3D}\right) \quad (8),$$

$$a = \frac{1}{2} + \frac{1}{6} \left[\exp\left(-\frac{GSI}{15}\right) + \exp\left(-\frac{20}{3}\right) \right] \quad (9).$$

GSI is the Geological Strength Index, a unitless value between 0 and 100 that describes the rock-mass characteristics (Marinos et al., 2005). High values of GSI represent intact or massive rock masses, whereas low GSI values represent blocky and fractured rock masses with weathered fracture surfaces and clay-filled fractures

(Marinos et al., 2005). D is a unitless disturbance factor related to anthropogenic blasting damage in large excavations (we therefore use $D = 0$ in our study; the full equation is provided here for completeness). Finally, unitless constant m_i describes the shape of the failure envelope on a graph of σ'_1 as a function of σ'_3 , and is therefore related to the microstructural and mineralogical attributes of the rock (Eberhardt, 2012).

To provide strengths for suevite rock masses, we require estimates for C_o , m_i , and GSI. Values of C_o can be taken directly from our experimental data, and we take values of 44.7 and 14.5 MPa for the SUE and AU1 suevites, respectively (excluding outliers). Values of m_i can be estimated using our triaxial experimental data. We estimate m_i , using the data fitting function (modified cuckoo fit algorithm, basic error summation, and absolute error type) in RocData (Rocscience, 2017), to be 12 and 4.7 for the SUE and AU1 suevites, respectively (Figure 14). In the absence of GSI estimates, we use the suggested average for volcanic rock masses of 55 suggested by Heap et al. (2020b). However, because of the variability in GSI values for natural outcrops (estimates of GSI for volcanic rock outcrops, for example, typically range between disintegrated (GSI = 20-40) and blocky (GSI = 65-85); see Heap et al., 2020b and references therein), we provide rock mass strength estimates for GSI = 45-65 (i.e., GSI = 55 ± 10). We can now model the compressive strength of SUE and AU1 as a function of depth (using $P = \rho gh$, where P is the lithostatic pressure, h is the depth, g is the acceleration due to gravity, and ρ is the bulk rock density (taken as 2000 kg/m^3 , guided by our laboratory density measurements)) (Figure 15). In the following analyses we provide strength estimates for rock masses on Mars (i.e., $g = 3.711 \text{ m/s}^2$).

We compare our strength estimations for SUE and AU1 with that for basalt (Figure 15), which is lithologically representative of much of the surface materials of the inner Solar System worlds (e.g., Byrne, 2019). To do so, we performed six uniaxial compressive strength experiments on dry samples of Volvic basalt (Chaîne des Puys, France). The connected porosity and uniaxial compressive strength of these samples were determined as described in the methods section. To estimate the strength of a basaltic rock-mass, we used a value of C_o of 92.6 MPa (Table 4), an m_i of 22 (see Schultz, 1995), and a GSI of 55 ± 10 (Heap et al., 2020b). We increased the bulk rock density from 2000 to 2300 kg/m³, as guided by our laboratory density measurements for Volvic basalt. We find that the upscaled compressive strength of suevite is much lower than that of basalt (Figure 15). For example, the rock-mass strength of SUE, AU1, and Volvic basalt are, respectively, ~11, ~25, and ~45 MPa at a depth of 0.5 km (Figure 15). Furthermore, the basalt will remain brittle over the range of depth (up to 5 km) shown in Figure 15; the suevites from Seelbronn (SUE) and Aumühle (AU1) will be ductile at depths of about 1 and 4 km, respectively (Figure 15). We note that, based on the depth of impact craters (e.g., Boyce et al., 2005; Stepinski et al., 2009), impact melt-bearing breccias are unlikely to exist below a couple of kilometres in the lithosphere. We further note that we use data for Volvic basalt for illustrative purposes: the porosity of basalt on Mars will certainly vary and its strength is very much porosity-dependent (e.g., Al-Harthi et al., 1999).

The Young's modulus of a fractured rock-mass, E_{rm} , can be estimated using the Hoek–Diederichs equation (Hoek and Diederichs, 2006):

$$E_{rm} = E_i \left[0.02 + \left(1 - \frac{D}{2} \left[1 + \exp \frac{(60 + 15D - GSI)}{11} \right]^{-1} \right) \right] \quad (10).$$

Here, E_i is the “intact” Young’s modulus measured from the elastic portion of the stress–strain curve of a rock deforming in compression (i.e., the data of Figure 7; Table 2). We take $D = 0$ (see above) and assume an average GSI of 55 (Heap et al., 2020b). We also determined the intact (Table 4) and rock-mass Young’s modulus for Volvic basalt. The data are presented in Figure 16 and show that the Young’s modulus of a rock-mass is much lower than intact Young’s modulus. For example, the range of Young’s modulus for SUE suevite was reduced from 3.5–8.1 to 1.4–3.3 GPa (Figure 16). These data also show that the intact and rock-mass Young’s modulus of suevite is much lower than that for basalt (Figure 16). Of course, the Young’s modulus of Volvic basalt represents that value of a basalt with a porosity of 0.2 (Table 4), but the porosity, and therefore Young’s modulus, of basalt on Mars likely varies considerably. As for our rock mass strength estimations, we can also provide rock mass Young’s modulus estimations for $\text{GSI} = 55 \pm 10$. The average rock mass Young’s moduli in this GSI range are 1.5–4.1, 1.3–3.6, 0.7–1.9, and 3.6–10.2 GPa for SUE, ALT, AU, and Volvic basalt, respectively.

The permeability of a rock-mass can be estimated if the macrofracture density and width, the permeability of the host-rock, and the permeability of the fractures is known (e.g., Heap and Kennedy, 2016). Once rock-mass permeabilities are known, these values can be used to estimate permeability on larger scales (e.g., Farquharson and Wadsworth, 2018). The permeability of a rock-mass, k_e , can be estimated using the following two-dimensional model that considers flow in parallel layers:

$$k_e = \frac{(w_i \cdot k_0) + (w_f \cdot k_f)}{W} \quad (11),$$

where w_i and k_0 and w_f and k_f and are the width and permeability of the intact host-rock and fractures, respectively, and W is the width of the rock-mass. If we take k_0 to be $5.0 \times 10^{-15} \text{ m}^2$ (Table 2), and assume a constant fracture width of 0.25 mm and a k_f of $1.0 \times 10^{-9} \text{ m}^2$ (see Heap and Kennedy, 2016), we can plot rock-mass permeability as a function of fracture density (Figure 17). To compare these data with those for basalt, we measured the permeability of one sample of Volvic basalt using the approach described in the methods section (Table 4). For the basalt calculations, we used $k_0 = 2.4 \times 10^{-14} \text{ m}^2$ (Table 4), and again assumed a constant fracture width of 0.25 mm and a k_f of $1.0 \times 10^{-9} \text{ m}^2$ (Figure 17). We assume a constant fracture width of 0.25 mm because this fracture width corresponds to the laboratory-measured value of k_f (see Heap and Kennedy, 2016). The permeability of large-aperture fractures is likely higher than the values of k_f provided herein, the permeability of which could be estimated using $k_f = h^2/12$ (Zimmerman and Bodvarsson, 1996), where h is the fracture width.

We find that, at very low fracture densities (between 0 and 2 fractures per metre), the basaltic rock-mass is more permeable than the suevite rock-mass (Figure 17). Above two fractures per metre, the equivalent permeabilities of the basalt and suevite rock masses are very similar (Figure 17). Figure 17 also shows that only a few macroscopic fractures per metre can increase the permeability of the rock-mass by two orders of magnitude. Above a macroscopic fracture density of about 10 fractures per metre, the equivalent permeability of the rock-mass does not increase significantly as a function of increasing fracture density (Figure 17). We emphasise that the permeability of basalt on the sample scale can be very low (e.g., 10^{-19} m^2 ; Nara et al., 2011) and will depend on both porosity and void-space connectivity. Therefore, the equivalent permeability of low porosity basalt on Mars may be considerably lower

than the estimates for Volvic basalt provided herein, especially at low macrofracture densities.

Although there are a number of assumptions built into our upscaling calculations (for strength, Young's modulus, and permeability), these calculations are designed to emphasise that care should be taken when deciding on physical property values for large-scale models.

4.7 Implications for impacted planetary bodies

Our findings show that suevites can have high porosities and low strength values (e.g., Figure 15), which is not surprising given the destructive nature of large impact events and the damage to rock masses that ensues (e.g., Morgan et al., 2016). For example, the compressive strength of suevite can be 2–4 times lower than that for basalt, a rock representative of much of the surface materials of the inner Solar System worlds (e.g., Byrne, 2019), at a depth of 0.5 km (for Mars; Figure 15). Our experiments also show that suevite will be ductile at shallow depths (Figure 8), which will likely affect, for example, the propagation of large fractures and dykes.

Most of inner Solar System worlds show evidence for protracted histories of impact bombardment. The “intercrater plains” on Mercury, which occupy ~75% of the planet surface (Whitten et al., 2014; Byrne et al., 2018), are heavily cratered and record more than 4 Gyr of impacts (Marchi et al., 2013). The southern uplands on Mars are similarly cratered and comparably old (Tanaka et al., 2014), as is much of the Moon's surface, especially the lunar highlands (e.g., Fassett et al., 2012b). Our study suggests that the rock masses that comprise these older, bombarded crusts are therefore substantially weaker and more porous and permeable than the younger plains material on these worlds, e.g., Mercury's smooth plains, the northern lowland

plains on Mars, and the lunar maria (cf. Byrne, 2019). Indeed, the difference in tectonic style of crustal shortening between the intercrater and smooth plains on Mercury has been attributed to the destruction, via impact bombardment, of any internal fabric in the former terrain type that the latter may still possess (Byrne et al., 2014). And although further weakening of crustal rocks by alteration likely did not have affect the airless bodies, e.g., Mercury or the Moon, such systems were probably present on Mars (Rathbun and Squyres, 2002; Osinski et al., 2013). (We exclude Venus from this discussion because the second planet has anomalously few impact craters (Phillips et al., 1991), and it not clear what effect(s) its high mean surface temperature ($\sim 470^\circ\text{C}$) might have had on those rocks that were impacted.)

In any case, our results here add to the few available data for the strength of planetary materials damaged by impact bombardment. It is therefore prudent to use such values in calculations of, for instance, the strength of the upper lithosphere of planetary bodies, when employing values for intact rock can lead to substantially different outcomes than for—more realistically—weak rock (e.g., Klimczak, 2015; Klimczak et al., 2015). Indeed, results from the NASA Gravity Recovery and Interior Laboratory (GRAIL) mission showed the Moon to have an average crustal porosity of 12% to a depth of at least several kilometres (Wieczorek et al., 2013), varying regionally to as much as 22%—comparable to those values we find for the Seelbronn (SUE) and Altenbürg (ALT) samples.

5 Conclusions

We provide here petrophysical property data (porosity, permeability, Young's modulus, and uniaxial compressive strength) for suevite (a type of melt-bearing impact breccia) from the Ries crater in Germany. We further performed triaxial

experiments to determine the pressure (i.e., depth) required for the brittle–ductile transition. Until now, petrophysical and mechanical data for melt-bearing impact breccia were rare or absent. It is our hope that these data, and our upscaling approaches, can improve fluid flow modelling, slope and crater stability assessments, crustal strength estimates, and physical weathering rate estimates for and the interpretation of large-scale structural features on planetary bodies on which protracted records of impact bombardment are preserved.

Acknowledgements

The first author acknowledges a Prix d’Espoirs grant, awarded by the University of Strasbourg. Olivier Lengliné is warmly thanked for driving the author to and from Nördlingen (Germany). Alexandra Kushnir is thanked for field assistance, Patrick Baud for discussions, Bertrand Renaudié for his help with the preparation of samples, and Marlène Villeneuve for determining the values of m_i using RocData. We thank Lea Mertens and Matthias Wittner for providing the suevite block from the Seelbronn quarry (Wittner - Steinbearbeitung und Denkmalpflege, Nördlingen, Germany). PKB acknowledges support from North Carolina State University. We thank Chris Okubo and one anonymous reviewer for comments that helped improve this manuscript.

Data availability

The data collected for this study can be found in Tables 1–4.

Figure captions

Figure 1. (a) Map of Germany showing the location of Nördlingen (in red). (b) Map showing the outer- (dashed line) and inner-ring (dotted line) of the Ries impact crater. The red circle shows the location of the town of Nördlingen. Green circles indicate the locations of the quarries from where the experimental materials were sourced (Aumühle, Altenbürg, and Seelbronn). (c) GoogleEarthTM image of the crater showing the location of Nördlingen. The crater is approximately 20 km in diameter.

Figure 2. Photographs of representative 25 mm-diameter cylindrical core samples prepared from the blocks collected. The symbol below each photograph corresponds to the symbols used in Figures 5, 6, and 7.

Figure 3. Backscattered electron microscope images of impact melt-bearing breccias (“suevites”) from each of the three quarry sites: (a) Seelbronn; (b) Altenbürg; and (c) Aumühle (see Figure 1 for locations). Panels (a) and (b) are taken from Heap et al. (2020a).

Figure 4. Cumulative void space as a function of the equivalent pore throat radius for impact melt-bearing breccias (“suevites”) from each of the three quarry sites: Seelbronn (SUE); Altenbürg (ALT); and Aumühle (AU1). (See Figure 1 for sample locations.)

Figure 5. Permeability as a function of connected porosity for impact melt-bearing breccias (“suevites”) from each of the three quarry sites (see Figure 1 for locations). “AU” includes samples from blocks AU1, AU2, and AU3 (see Table 2).

Figure 6. (a) Representative uniaxial stress–strain curves for impact melt-bearing breccias (“suevites”) from each of the three quarry sites (see Figure 1 for locations). The peak stress is labelled for the SUE curve. Sections OA, AB, and BC on the SUE curve indicate the different parts of a typical stress–strain curve (see text for details). (b) Uniaxial compressive strength as a function of connected porosity for these samples. “AU” includes samples from blocks AU1, AU2, and AU3 (see Table 2).

Figure 7. Static Young’s modulus as a function of connected porosity for impact melt-bearing breccias (“suevites”) from each of the three quarry sites (see Figure 1 for locations). “AU” includes samples from blocks AU1, AU2, and AU3 (see Table 2).

Figure 8. (a) Stress–strain curves for the impact melt-bearing breccias (“suevites”) from Seelbronn (SUE) (see Figure 1 for location). (b) Stress–strain curves for the samples from the Aumühle (AU1) quarry (see Figure 1 for location). In both plots, the effective pressure (P_{eff}) for each experiment is labelled next to the appropriate curve.

Figure 9. Backscattered electron microscope images of deformed samples of impact melt-bearing breccias (“suevites”) from the Seelbronn quarry (SUE) (see Figure 1 for location). Panels (a) and (b) show shear fractures (and accompanying microcracks) resulting from brittle failure. Panels (c) and (d) show the micromechanism driving

porosity loss during the ductile experiments: cataclastic pore collapse (and accompanying microcracks).

Figure 10. Permeability as a function of connected porosity for impact melt-bearing breccias (“suevites”) from each of the three quarry sites (see Figure 1 for locations). “AU” includes samples from blocks AU1, AU2, and AU3 (see Table 2). The dashed line is the modelled curve (Equation (2)).

Figure 11. Uniaxial compressive strength as a function of connected porosity for impact melt-bearing breccias (“suevites”) from each of the three quarry sites. “AU” includes samples from blocks AU1, AU2, and AU3 (see Table 2). Modelled curves are provided using the analytical approximation of Sammis and Ashby’s (1986) pore-emanating crack model (Equation (3)).

Figure 12. Differential stress, Q , (peak stress in the brittle regime and C^* in the ductile regime) as a function of the effective mean stress, P , for impact melt-bearing breccias (“suevites”) from Seelbronn (SUE) and Aumühle (AU1) (see Figure 1 for location) (data given in Table 3).

Figure 13. (a) The onset of inelastic hydrostatic compaction, P^* , as a function of the uniaxial compressive strength for the impact melt-bearing breccias (“suevites”) from Seelbronn (SUE) and Aumühle (AU1) (see Figure 1 for location). The position of P^* for SUE and AU1 is estimated to be 90 ± 5 and 22 ± 5 MPa. The modelled curve is provided using Equation (4). (b) The onset of inelastic hydrostatic compaction, P^* , as a function of porosity for SUE and AU1 samples. The position of P^* for SUE and

AU1 is estimated to be 90 ± 5 and 22 ± 5 MPa (symbol size is larger than the error bar). Modelled curves are provided using Equation (5). On both panels we also provide data for tuff, a volcanic rock with a similar texture to the studied suevites (data from Heard et al., 1973; Aversa and Evangelista, 1998; Lockner and Morrow, 2008; Zhu et al., 2011; Heap et al., 2014b; Marmoni et al., 2017; Heap et al., 2018).

Figure 14. Data from triaxial experiments performed on samples of impact melt-bearing breccias (“suevites”) from Seelbronn (SUE) and Aumühle (AU1) (see Figure 1 for location) plotted in principal stress space (major principal stress as a function of minor principal stress). Best-fit modelled curves are provided using the data fitting function (modified cuckoo fit algorithm, basic error summation, and absolute error type) in RocData (Rocscience, 2017). The best-fit m_i values are given on the figure.

Figure 15. Crustal strength profiles (for Mars) for impact melt-bearing breccias (“suevites”) from Seelbronn (SUE) and Aumühle (AU1), (see Figure 1 for location) and for Volvic basalt (Chaîne des Puys, France), calculated with Equation (6). Dashed lines indicate the depth range for ductile deformation, as informed by our experimental data (Table 3); strength values provided by Equation (6) are not valid for this depth range. Solid/dashed lines are for a Geological Strength Index (GSI) of 55 and the shaded zones show strength profiles for $GSI = 55 \pm 10$ (see text for details).

Figure 16. “Intact” (coloured symbols) and rock-mass (white symbols) Young’s modulus as a function of connected porosity for impact melt-bearing breccias (“suevites”) from Seelbronn (SUE), Altenbürg (ALT), and Aumühle (AU1) (see

Figure 1 for locations) and for Volvic basalt (Chaîne des Puys, France). Rock-mass Young's moduli are calculated using Equation (10) and using a GSI of 55.

Figure 17. Equivalent permeability as a function of macrofracture density for impact melt-bearing breccia ("suevite"), calculated using Equation (11).

Table 1. Quantitative bulk mineralogical composition, determined using X-ray powder diffraction (XRPD), for the five impact melt-bearing breccias (“suevite”) blocks used in this study. The error associated with the estimation of the content of amorphous phases is a conservative estimate. “n.d.”: not detected.

Mineral	Altenbürg (ALT) (values in wt.%)	Seelbronn (SUE) (values in wt.%)	Aumühle 1 (AU1) (values in wt.%)	Aumühle 2 (AU2) (values in wt.%)	Aumühle 3 (AU3) (values in wt.%)
Quartz	9 ± 1	10 ± 1	11 ± 1	11 ± 1	11 ± 1
Coesite	1.7 ± 0.3	1.4 ± 0.3	0.7 ± 0.2	0.8 ± 0.2	0.9 ± 0.2
K-feldspar	3.1 ± 0.5	1.7 ± 0.5	4.5 ± 0.8	3.5 ± 0.5	4.3 ± 0.4
Plagioclase	18 ± 2	27 ± 3	17 ± 2	16 ± 2	15 ± 2
Calcite	13 ± 1	2.1 ± 0.2	2.6 ± 1.2	1.1 ± 1.2	0.6 ± 0.3
Smectite	25 ± 3	23 ± 3	31 ± 4	34 ± 4	37 ± 4
Amphibole	1.7 ± 0.3	n.d.	n.d.	n.d.	n.d.
Biotite	2.0 ± 0.5	1.9 ± 0.5	1.8 ± 0.5	1.8 ± 0.5	1.9 ± 0.5
Hematite/Goethite	0.2 ± 0.1	0.2 ± 0.1	0.4 ± 0.2	0.4 ± 0.2	0.2 ± 0.2
Amorphous phases	28 ± 5	33 ± 5	32 ± 8	32 ± 8	30 ± 8

Table 2. The physical and mechanical properties (porosity, permeability, Young's modulus, and uniaxial compressive strength) of dry impact melt-bearing breccia ("suevite") collected from the Ries impact crater, Germany. Asterisk denotes data from Heap et al. (2020a).

Sample	Connected porosity	Permeability (m ²)	Young's modulus (GPa)	Uniaxial compressive strength (MPa)
SUE1*	0.241	6.33×10^{-15}	3.5	18.4
SUE2*	0.197	6.22×10^{-16}	8.1	48.6
SUE3*	0.238	5.68×10^{-15}	-	-
SUE4*	0.221	7.40×10^{-16}	4.7	21.7
SUE5*	0.190	9.53×10^{-16}	7.9	42.2
SUE6*	0.184	1.08×10^{-15}	-	-
SUE7*	0.197	1.42×10^{-15}	-	-
SUE8*	0.204	6.32×10^{-16}	6.4	32.8
SUE9*	0.240	1.47×10^{-15}	-	-
SUE10*	0.198	5.84×10^{-16}	7.7	43.3
SUE12*	0.195	-	6.2	32.8
SUE20*	0.228	-	7.6	34.1
ALT1*	0.242	1.02×10^{-15}	6.1	31.7
ALT2*	0.261	2.54×10^{-15}	-	31.6
ALT3*	0.261	2.44×10^{-15}	-	-
ALT4*	0.233	3.13×10^{-15}	5.7	25.3
ALT5*	0.243	1.76×10^{-15}	-	-
ALT6*	0.262	3.16×10^{-15}	5.0	17.7
ALT7*	0.238	1.19×10^{-15}	-	-
ALT8*	0.261	1.84×10^{-15}	4.3	22.5
ALT9*	0.261	2.13×10^{-15}	-	-
ALT10*	0.231	9.54×10^{-16}	7.1	33.0
ALT12*	0.245	-	6.1	34.8
ALT13*	0.223	-	6.3	33.6
ALT14*	0.242	-	6.1	34.6
ALT15*	0.248	-	4.8	26.9
AU1_1	0.387	4.78×10^{-15}	3.4	14.7
AU1_2	0.392	5.66×10^{-15}	3.6	15.0
AU1_3	0.388	5.38×10^{-15}	3.7	15.0
AU1_4	0.384	1.57×10^{-14}	3.9	15.7
AU1_5	0.386	6.59×10^{-15}	2.9	14.0
AU1_6	0.380	4.29×10^{-15}	4.1	15.0
AU1_7	0.396	4.53×10^{-15}	3.3	14.3

AU1_8	0.389	5.30×10^{-15}	2.9	12.6
AU1_9	0.390	6.02×10^{-15}	3.4	14.0
AU1_10	0.380	5.97×10^{-15}	3.3	14.8
AU1_11	0.388	4.77×10^{-15}	3.5	14.2
AU2_1	0.383	5.24×10^{-15}	3.4	13.1
AU2_2	0.381	2.37×10^{-15}	3.7	16.6
AU2_3	0.370	3.05×10^{-15}	3.4	15.5
AU2_4	0.408	4.10×10^{-15}	1.4	7.3
AU2_5	0.401	4.08×10^{-15}	2.5	10.8
AU2_6	0.382	4.00×10^{-15}	3.5	14.0
AU2_7	0.380	4.11×10^{-15}	3.4	14.5
AU2_8	0.381	6.43×10^{-15}	2.8	9.4
AU2_9	0.369	3.46×10^{-15}	3.3	15.2
AU2_10	0.385	3.79×10^{-15}	2.7	11.7
AU2_11	0.370	3.35×10^{-15}	2.9	14.8
AU2_12	0.362	3.40×10^{-15}	3.2	15.8
AU3_1	0.397	1.06×10^{-14}	2.3	9.7
AU3_2	0.417	5.10×10^{-14}	2.0	8.2
AU3_3	0.399	9.96×10^{-15}	2.6	10.3
AU3_4	0.434	1.44×10^{-14}	2.6	8.7
AU3_5	0.382	4.78×10^{-15}	3.0	11.5
AU3_6	0.412	1.94×10^{-14}	2.4	10.4
AU3_7	0.407	1.63×10^{-14}	2.2	10.2
AU3_8	0.401	1.15×10^{-14}	2.6	11.8

Table 3. Mechanical data from the triaxial deformation experiments on dry impact melt-bearing breccia (“suevite”) performed for this study. The asterisk denotes samples that were held at a differential stress of 2 MPa and the confining pressure was increased until C^* was reached (see methods section for more details).

Sample	Connected porosity	Confining pressure (MPa)	Pore fluid pressure (MPa)	Effective pressure (MPa)	Peak differential stress, Q (MPa)	C^* (MPa)	Effective mean stress, P (MPa)
SS2	0.252	5	0	5	69.9	-	28.3
SS3	0.242	10	0	10	75.1	-	35.0
SS4	0.255	15	0	15	99.2	-	48.1
SS6	0.246	20	0	20	94.6	-	51.5
SS7	0.251	30	0	30	-	74.5	54.8
SS8	0.252	50	0	50	-	54.9	68.3
SS10*	0.247	90	0	90	-	2.0	90.7
SS11	0.234	80	0	80	-	24.7	88.2
SS12	0.237	10	0	10	97.9	-	41.6
AU1_1	0.376	5	0	5	23.9	-	13.0
AU1_3	0.383	10	0	10	-	17.1	15.7
AU1_7	0.385	15	0	15	-	12.2	19.1
AU1_11	0.385	20	0	20	-	7.6	22.5
AU1_12	0.377	2.5	0	2.5	18.5	-	8.7
AU1_16*	0.384	22	0	22	-	2.0	22.7

Table 4. The physical and mechanical properties (porosity, permeability, Young's modulus, and uniaxial compressive strength) of dry Volvic basalt (Chaîne des Puys, France). Asterisk denotes data from Heap et al. (2020b).

Sample	Connected porosity	Permeability (m ²)	Young's modulus (GPa)	Uniaxial compressive strength (MPa)
VB2	0.20	2.35×10^{-14}	17.1*	94.6
VB6	0.21	-	15.4*	96.5
VB8	0.20	-	16.8*	84.2
VB9	0.21	-	15.2*	91.1
VB10	0.21	-	16.1*	94.8
VB12	0.21	-	16.1*	94.7

References

- Aben, F. M., Brantut, N., Mitchell, T. M., & David, E. C. Rupture energetics in crustal rock from laboratory-scale seismic tomography. *Geophysical Research Letters*.
- Abramov, O., & Kring, D. A. (2004). Numerical modeling of an impact-induced hydrothermal system at the Sudbury crater. *Journal of Geophysical Research: Planets*, 109(E10).
- Abramov, O., & Kring, D. A. (2005). Impact-induced hydrothermal activity on early Mars. *Journal of Geophysical Research: Planets*, 110(E12).
- Abramov, O., & Kring, D. A. (2007). Numerical modeling of impact-induced hydrothermal activity at the Chicxulub crater. *Meteoritics & Planetary Science*, 42(1), 93-112.
- Adelinet, M., Fortin, J., Schubnel, A., & Guéguen, Y. (2013). Deformation modes in an Icelandic basalt: from brittle failure to localized deformation bands. *Journal of Volcanology and Geothermal Research*, 255, 15-25.
- Al-Harthi, A. A., Al-Amri, R. M., & Shehata, W. M. (1999). The porosity and engineering properties of vesicular basalt in Saudi Arabia. *Engineering Geology*, 54(3-4), 313-320.
- Andrews-Hanna, J. C., & Phillips, R. J. (2007). Hydrological modeling of outflow channels and chaos regions on Mars. *Journal of Geophysical Research: Planets*, 112(E8).
- Aversa, S., & Evangelista, A. (1998). The mechanical behaviour of a pyroclastic rock: yield strength and “destruction” effects. *Rock Mechanics and Rock Engineering*, 31(1), 25-42.
- Baud, P., Klein, E., & Wong, T. F. (2004). Compaction localization in porous sandstones: spatial evolution of damage and acoustic emission activity. *Journal of Structural Geology*, 26(4), 603-624.
- Baud, P., Vajdova, V., & Wong, T. F. (2006). Shear-enhanced compaction and strain localization: Inelastic deformation and constitutive modeling of four porous sandstones. *Journal of Geophysical Research: Solid Earth*, 111(B12).
- Baud, P., Wong, T. F., & Zhu, W. (2014). Effects of porosity and crack density on the compressive strength of rocks. *International Journal of Rock Mechanics and Mining Sciences*, 67, 202-211.
- Baud, P., Reuschlé, T., Ji, Y., Cheung, C. S., & Wong, T. F. (2015). Mechanical compaction and strain localization in Bleurswiller sandstone. *Journal of Geophysical Research: Solid Earth*, 120(9), 6501-6522.
- Baud, P., Schubnel, A., Heap, M., & Rolland, A. (2017). Inelastic Compaction in High-Porosity Limestone Monitored Using Acoustic Emissions. *Journal of Geophysical Research: Solid Earth*, 122(12), 9989-10.
- Barnhart, C. J., Nimmo, F., & Travis, B. J. (2010). Martian post-impact hydrothermal systems incorporating freezing. *Icarus*, 208(1), 101-117.
- Barnouin, O. S., Zuber, M. T., Smith, D. E., Neumann, G. A., Herrick, R. R., Chappelow, J. E., ... & Prockter, L. M. (2012). The morphology of craters on Mercury: Results from MESSENGER flybys. *Icarus*, 219(1), 414-427.
- Bergmann, J., Friedel, P., & Kleeberg, R. (1998). BGMN—a new fundamental parameters based Rietveld program for laboratory X-ray sources, its use in quantitative analysis and structure investigations. *CPD Newsletter*, 20(5).
- Boyce, J. M., Mouginis-Mark, P., & Garbeil, H. (2005). Ancient oceans in the northern lowlands of Mars: Evidence from impact crater depth/diameter relationships. *Journal of Geophysical Research: Planets*, 110(E3).
- Brace, W. F. (1984). Permeability of crystalline rocks: New in situ measurements. *Journal of Geophysical Research: Solid Earth*, 89(B6), 4327-4330.
- Brunetti, M. T., Guzzetti, F., Cardinali, M., Fiorucci, F., Santangelo, M., Mancinelli, P., ... & Borselli, L. (2014). Analysis of a new geomorphological inventory of landslides in Valles Marineris, Mars. *Earth and Planetary Science Letters*, 405, 156-168.
- Byrne, P. K., Klimczak, C., Sengor, A. M. C., Solomon, S. C., Watters, T. R., & Hauck II, S. A. (2014). Mercury: global tectonics on a contracting planet. *Nat. Geosci.*, 7, 301-307.
- Byrne, P. K., Klimczak, C., & Şengör, A. M. C. (2018). The tectonic character of Mercury. *Mercury: The View After MESSENGER*.
- Byrne, P. K. (2019). A comparison of inner Solar System volcanism. *Nature Astronomy*, 1-7.
- Chang, C., Zoback, M. D., & Khaksar, A. (2006). Empirical relations between rock strength and physical properties in sedimentary rocks. *Journal of Petroleum Science and Engineering*, 51(3-4), 223-237.
- Cheung, C. S., Baud, P., & Wong, T. F. (2012). Effect of grain size distribution on the development of compaction localization in porous sandstone. *Geophysical Research Letters*, 39(21).

- Cilona, A., Faulkner, D. R., Tondi, E., Agosta, F., Mancini, L., Rustichelli, A., ... & Vinciguerra, S. (2014). The effects of rock heterogeneity on compaction localization in porous carbonates. *Journal of Structural Geology*, 67, 75-93.
- Clauser, C. (1992). Permeability of crystalline rocks. *Eos, Transactions American Geophysical Union*, 73(21), 233-238.
- Collins, G. S. (2014). Numerical simulations of impact crater formation with dilatancy. *Journal of Geophysical Research: Planets*, 119(12), 2600-2619.
- Christeson, G. L., Gulick, S. P. S., Morgan, J. V., Gebhardt, C., Kring, D. A., Le Ber, E., ... & Rebolledo-Vieyra, M. (2018). Extraordinary rocks from the peak ring of the Chicxulub impact crater: P-wave velocity, density, and porosity measurements from IODP/ICDP Expedition 364. *Earth and Planetary Science Letters*, 495, 1-11.
- del Potro, R., & Hürlimann, M. (2009). The decrease in the shear strength of volcanic materials with argillic hydrothermal alteration, insights from the summit region of Teide stratovolcano, Tenerife. *Engineering Geology*, 104(1-2), 135-143.
- Döbelin, N. & Kleeberg, R. (2015) Profex: a graphical user interface for the Rietveld refinement program BGMN. *Journal of Applied Crystallography*, 48(5), 1573-1580
- Durán, E. L., Adam, L., Wallis, I. C., & Barnhoorn, A. (2019). Mineral alteration and fracture influence on the elastic properties of volcanoclastic rocks. *Journal of Geophysical Research: Solid Earth*, 124(5), 4576-4600.
- Eberhardt, E. (2012). The hoek–brown failure criterion. *Rock Mechanics and Rock Engineering*, 45(6), 981-988.
- Elbra, T., & Pesonen, L. J. (2011). Physical properties of the Yaxcopoil-1 deep drill core, Chicxulub impact structure, Mexico. *Meteoritics & Planetary Science*, 46(11), 1640-1652.
- Eppes, M. C., Willis, A., Molaro, J., Abernathy, S., & Zhou, B. (2015). Cracks in Martian boulders exhibit preferred orientations that point to solar-induced thermal stress. *Nature Communications*, 6, 6712.
- Etioppe, G., Ehlmann, B. L., & Schoell, M. (2013). Low temperature production and exhalation of methane from serpentinized rocks on Earth: a potential analog for methane production on Mars. *Icarus*, 224(2), 276-285.
- Farquharson, J., Heap, M. J., Varley, N. R., Baud, P., & Reuschlé, T. (2015). Permeability and porosity relationships of edifice-forming andesites: a combined field and laboratory study. *Journal of Volcanology and Geothermal Research*, 297, 52-68.
- Farquharson, J. I., Heap, M. J., Lavallée, Y., Varley, N. R., & Baud, P. (2016). Evidence for the development of permeability anisotropy in lava domes and volcanic conduits. *Journal of Volcanology and Geothermal Research*, 323, 163-185.
- Farquharson, J. I., Baud, P., & Heap, M. J. (2017). Inelastic compaction and permeability evolution in volcanic rock. *Solid Earth*, 8(2), 561-581.
- Farquharson, J. I., & Wadsworth, F. B. (2018). Upscaling permeability in anisotropic volcanic systems. *Journal of Volcanology and Geothermal Research*, 364, 35-47.
- Fassett, C. I., Head, J. W., Baker, D. M., Zuber, M. T., Smith, D. E., Neumann, G. A., ... & Prockter, L. M. (2012a). Large impact basins on Mercury: Global distribution, characteristics, and modification history from MESSENGER orbital data. *Journal of Geophysical Research: Planets*, 117(E12).
- Fassett, C. I., Head, J. W., Kadish, S. J., Mazarico, E., Neumann, G. A., Smith, D. E., & Zuber, M. T. (2012b). Lunar impact basins: Stratigraphy, sequence and ages from superposed impact crater populations measured from Lunar Orbiter Laser Altimeter (LOLA) data. *Journal of Geophysical Research: Planets*, 117(E12).
- Forchheimer, P. (1901). Wasserbewegung durch boden. *Z. Ver. Deutsch, Ing.*, 45, 1782-1788.
- Fortin, J., Stanchits, S., Dresen, G., & Guéguen, Y. (2006). Acoustic emission and velocities associated with the formation of compaction bands in sandstone. *Journal of Geophysical Research: Solid Earth*, 111(B10).
- Frolova, F., Ladygin, V., Rychagov, S., & Zukhubaya, D. (2014). Effects of hydrothermal alterations on physical and mechanical properties of rocks in the Kuril–Kamchatka island arc. *Engineering geology*, 183, 80-95.
- Graup, G. (1981). Terrestrial chondrules, glass spherules and accretionary lapilli from the suevite, Ries Crater, Germany. *Earth and Planetary Science Letters*, 55, 407-418.
- Grieve, R. A., & Shoemaker, E. M. (1994). The record of past impacts on Earth. *Hazards due to Comets and Asteroids*, 417-462.
- Grimm, R. E., & Painter, S. L. (2009). On the secular evolution of groundwater on Mars. *Geophysical Research Letters*, 36(24).

- Gulick, V. C. (1998). Magmatic intrusions and a hydrothermal origin for fluvial valleys on Mars. *Journal of Geophysical Research: Planets*, 103(E8), 19365-19387.
- Halperin, B. I., Feng, S., & Sen, P. N. (1985). Differences between lattice and continuum percolation transport exponents. *Physical Review Letters*, 54(22), 2391.
- Harnett, C. E., Kendrick, J. E., Lamur, A., Thomas, M. E., Stinton, A., Wallace, P. A., ... & Lavallée, Y. (2019). Evolution of Mechanical Properties of Lava Dome Rocks Across the 1995–2010 Eruption of Soufrière Hills Volcano, Montserrat. *Frontiers in Earth Science*, 7.
- Harrison, K. P., & Grimm, R. E. (2009). Regionally compartmented groundwater flow on Mars. *Journal of Geophysical Research: Planets*, 114(E4).
- Heap, M. J., Xu, T., & Chen, C. F. (2014a). The influence of porosity and vesicle size on the brittle strength of volcanic rocks and magma. *Bulletin of Volcanology*, 76(9), 856.
- Heap, M. J., Baud, P., Meredith, P. G., Vinciguerra, S., & Reuschlé, T. (2014b). The permeability and elastic moduli of tuff from Campi Flegrei, Italy: implications for ground deformation modelling. *Solid Earth*, 5(1), 25-44.
- Heap, M. J., Farquharson, J. I., Wadsworth, F. B., Kolzenburg, S., & Russell, J. K. (2015a). Timescales for permeability reduction and strength recovery in densifying magma. *Earth and Planetary Science Letters*, 429, 223-233.
- Heap, M. J., Farquharson, J. I., Baud, P., Lavallée, Y., & Reuschlé, T. (2015b). Fracture and compaction of andesite in a volcanic edifice. *Bulletin of Volcanology*, 77(6), 55.
- Heap, M. J., Kennedy, B. M., Pernin, N., Jacquemard, L., Baud, P., Farquharson, J. I., ... & Mayer, K. (2015c). Mechanical behaviour and failure modes in the Whakaari (White Island volcano) hydrothermal system, New Zealand. *Journal of Volcanology and Geothermal Research*, 295, 26-42.
- Heap, M. J., & Kennedy, B. M. (2016). Exploring the scale-dependent permeability of fractured andesite. *Earth and Planetary Science Letters*, 447, 139-150.
- Heap, M. J., Violay, M., Wadsworth, F. B., & Vasseur, J. (2017a). From rock to magma and back again: The evolution of temperature and deformation mechanism in conduit margin zones. *Earth and Planetary Science Letters*, 463, 92-100.
- Heap, M. J., Byrne, P. K., & Mikhail, S. (2017b). Low surface gravitational acceleration of Mars results in a thick and weak lithosphere: Implications for topography, volcanism, and hydrology. *Icarus*, 281, 103-114.
- Heap, M., Kushnir, A., Griffiths, L., Wadsworth, F., Marmoni, G. M., Fiorucci, M., ... & Reuschlé, T. (2018). Fire resistance of the Mt. Epomeo Green Tuff, a widely-used building stone on Ischia Island (Italy). *Volcanica*, 1(1), 33-48. doi: 10.30909/vol.01.01.3348.
- Heap, M. J., Tuffen, H., Wadsworth, F. B., Reuschlé, T., Castro, J. M., & Schipper, C. I. (2019). The permeability evolution of tuffisites and implications for outgassing through dense rhyolitic magma. *Journal of Geophysical Research: Solid Earth*, 124(8), 8281-8299.
- Heap, M. J., Gilg, H. A., Hess, K. U., Mertens, L., Pösges, G., & Reuschlé, T. (2020a). Conservation and restoration of St. George's church (Nördlingen, Germany), a 15th century Gothic church built using suevite from the Ries impact crater. *Journal of Cultural Heritage*.
- Heap, M. J., Villeneuve, M., Albino, F., Farquharson, J. I., Brothelande, E., Amelung, F., ... & Baud, P. (2020b). Towards more realistic values of elastic moduli for volcano modelling. *Journal of Volcanology and Geothermal Research*, 106684.
- Heard, H. C., Bonner, B. P., Duba, A. G., Schock, R. N., & Stephens, D. R. (1973). *High-pressure mechanical properties of Mt. Helen, Nevada, tuff* (No. UCID-16261).
- Hoek, E., Carranza-Torres, C., & Corkum, B. (2002). Hoek-Brown failure criterion-2002 edition. *Proceedings of NARMS-Tac*, 1(1), 267-273.
- Hoek, E., & Diederichs, M. S. (2006). Empirical estimation of rock mass modulus. *International Journal of Rock Mechanics and Mining Sciences*, 43(2), 203-215.
- Hörz, F., Ostertag, R., & Rainey, D. A. (1983). Bunte Breccia of the Ries: Continuous deposits of large impact craters. *Reviews of Geophysics*, 21(8), 1667-1725.
- Huang, L., Baud, P., Cordonnier, B., Renard, F., Liu, L., & Wong, T. F. (2019). Synchrotron X-ray imaging in 4D: Multiscale failure and compaction localization in triaxially compressed porous limestone. *Earth and Planetary Science Letters*, 528, 115831.
- Kirsimäe, K., & Osinski, G. R. (2013). Impact-induced hydrothermal activity. *Impact Cratering: Processes and Products, first ed. Wiley-Blackwell, New Jersey*, 76-89.
- Klimczak, C. (2015). Limits on the brittle strength of planetary lithospheres undergoing global contraction. *Journal of Geophysical Research: Planets*, 120(12), 2135-2151.
- Klimczak, C., Byrne, P. K., & Solomon, S. C. (2015). A rock-mechanical assessment of Mercury's global tectonic fabric. *Earth and Planetary Science Letters*, 416, 82-90.

- Klinkenberg, L. J. (1941). The permeability of porous media to liquids and gases. In *Drilling and Production Practice*. American Petroleum Institute.
- Loaiza, S., Fortin, J., Schubnel, A., Gueguen, Y., Vinciguerra, S., & Moreira, M. (2012). Mechanical behavior and localized failure modes in a porous basalt from the Azores. *Geophysical Research Letters*, 39(19).
- Lockner, D., Byerlee, J. D., Kuksenko, V., Ponomarev, A., & Sidorin, A. (1991). Quasi-static fault growth and shear fracture energy in granite. *Nature*, 350(6313), 39.
- Lockner, D. A., & Morrow, C. A. (2008). Energy dissipation in Calico Hills tuff due to pore collapse. In *AGU Fall Meeting Abstracts*, Abstract T51A-1856.
- Lognonné, P., Banerdt, W. B., Pike, W. T., Giardini, D., Christensen, U., Garcia, R. F., ... & Nimmo, F. (2020). Constraints on the shallow elastic and anelastic structure of Mars from InSight seismic data. *Nature Geoscience*, 1-8.
- Lyons, J. R., Manning, C., & Nimmo, F. (2005). Formation of methane on Mars by fluid-rock interaction in the crust. *Geophysical Research Letters*, 32(13).
- Manga, M. (2004). Martian floods at Cerberus Fossae can be produced by groundwater discharge. *Geophysical Research Letters*, 31(2).
- Marchi, S., Chapman, C. R., Fassett, C. I., Head, J. W., Bottke, W. F., & Strom, R. G. (2013). Global resurfacing of Mercury 4.0–4.1 billion years ago by heavy bombardment and volcanism. *Nature*, 499(7456), 59-61.
- Marinos, V. I. I., Marinos, P., & Hoek, E. (2005). The geological strength index: applications and limitations. *Bulletin of Engineering Geology and the Environment*, 64(1), 55-65.
- Marmoni, G. M., Martino, S., Heap, M. J., & Reuschlé, T. (2017). Gravitational slope-deformation of a resurgent caldera: New insights from the mechanical behaviour of Mt. Nuovo tuffs (Ischia Island, Italy). *Journal of Volcanology and Geothermal Research*, 345, 1-20.
- Martys, N. S., Torquato, S., & Bentz, D. P. (1994). Universal scaling of fluid permeability for sphere packings. *Physical Review E*, 50(1), 403.
- Mayr, S. I., Wittmann, A., Burkhardt, H., Popov, Y., Romushkevich, R., Bayuk, I., ... & Wilhelm, H. (2008a). Integrated interpretation of physical properties of rocks of the borehole Yaxcopoil-1 (Chicxulub impact structure). *Journal of Geophysical Research: Solid Earth*, 113(B7).
- Mayr, S. I., Burkhardt, H., Popov, Y., & Wittmann, A. (2008b). Estimation of hydraulic permeability considering the micro morphology of rocks of the borehole YAXCOPOIL-1 (Impact crater Chicxulub, Mexico). *International Journal of Earth Sciences*, 97(2), 385-399.
- Melosh, H. J. (1989). Impact cratering: A geologic process. *Research supported by NASA. New York, Oxford University Press (Oxford Monographs on Geology and Geophysics, No. 11), 1989, 253 p., 11.*
- Melosh, H. J., & Ivanov, B. A. (1999). Impact crater collapse. *Annual Review of Earth and Planetary Sciences*, 27(1), 385-415.
- Mordensky, S. P., Villeneuve, M. C., Kennedy, B. M., Heap, M. J., Gravley, D. M., Farquharson, J. I., & Reuschlé, T. (2018). Physical and mechanical property relationships of a shallow intrusion and volcanic host rock, Pinnacle Ridge, Mt. Ruapehu, New Zealand. *Journal of Volcanology and Geothermal Research*, 359, 1-20.
- Morgan, J. V., Gulick, S. P., Bralower, T., Chenot, E., Christeson, G., Claeys, P., ... & Gebhardt, C. (2016). The formation of peak rings in large impact craters. *Science*, 354(6314), 878-882.
- Musioli, S., Cailleau, B., Platz, T., Kneissl, T., Dumke, A., & Neukum, G. (2011). Outflow activity near Hadriaca Patera, Mars: Fluid-tectonic interaction investigated with High Resolution Stereo Camera stereo data and finite element modeling. *Journal of Geophysical Research: Planets*, 116(E8).
- Muttik, N., Kirsimaee, K., Somelar, P., & Osinski, G. R. (2008). Post-impact alteration of surficial suevites in Ries crater, Germany: Hydrothermal modification or weathering processes? *Meteoritics & Planetary Science*, 43(11), 1827-1840.
- Muttik, N., Kirsimäe, K., & Vennemann, T. W. (2010). Stable isotope composition of smectite in suevites at the Ries crater, Germany: Implications for hydrous alteration of impactites. *Earth and Planetary Science Letters*, 299(1-2), 190-195.
- Muttik, N., Kirsimäe, K., Newsom, H. E., & Williams, L. B. (2011). Boron isotope composition of secondary smectite in suevites at the Ries crater, Germany: boron fractionation in weathering and hydrothermal processes. *Earth and Planetary Science Letters*, 310(3-4), 244-251.
- Neukum, G., König, B., & Arkani-Hamed, J. (1975). A study of lunar impact crater size-distributions. *The Moon*, 12(2), 201-229.
- Neuffer, D. P., & Schultz, R. A. (2006). Mechanisms of slope failure in Valles Marineris, Mars. *Quarterly Journal of Engineering Geology and Hydrogeology*, 39(3), 227-240.

- Neuman, S. P. (1994). Generalized scaling of permeabilities: Validation and effect of support scale. *Geophysical Research Letters*, 21(5), 349-352.
- Newsom, H. E., Graup, G., Sowards, T., & Keil, K. (1986). Fluidization and hydrothermal alteration of the suevite deposit at the Ries crater, West Germany, and implications for Mars. *Journal of Geophysical Research: Solid Earth*, 91(B13), E239-E251.
- Newsom, H. E., Graup, G., Iseri, D. A., Geissman, J. W., & Keil, K. (1990). The formation of the Ries crater, West Germany: Evidence of atmospheric interactions during a larger cratering event. In *Global catastrophes in Earth history: An interdisciplinary conference on impacts, volcanism, and mass mortality* (pp. 195-205). Geological Society of America.
- Okubo, C. H., Tornabene, L. L., & Lanza, N. L. (2011). Constraints on mechanisms for the growth of gully alcoves in Gasa crater, Mars, from two-dimensional stability assessments of rock slopes. *Icarus*, 211(1), 207-221.
- Osinski, G. R. (2003). Impact glasses in fallout suevites from the Ries impact structure, Germany: An analytical SEM study. *Meteoritics & Planetary Science*, 38(11), 1641-1667.
- Osinski, G. R., Grieve, R. A., & Spray, J. G. (2004). The nature of the groundmass of surficial suevite from the Ries impact structure, Germany, and constraints on its origin. *Meteoritics & Planetary Science*, 39(10), 1655-1683.
- Osinski, G. R. (2005). Hydrothermal activity associated with the Ries impact event, Germany. *Geofluids*, 5(3), 202-220.
- Osinski, G. R., Tornabene, L. L., & Grieve, R. A. (2011). Impact ejecta emplacement on terrestrial planets. *Earth and Planetary Science Letters*, 310(3-4), 167-181.
- Osinski, G. R., & Pierazzo, E. (2013). Impact cratering: Processes and products. *Impact Cratering*, 1-20.
- Osinski, G. R., Tornabene, L. L., Banerjee, N. R., Cockell, C. S., Flemming, R., Izawa, M. R., ... & Pontefract, A. (2013). Impact-generated hydrothermal systems on Earth and Mars. *Icarus*, 224(2), 347-363.
- Parmentier, E. M., & Zuber, M. T. (2007). Early evolution of Mars with mantle compositional stratification or hydrothermal crustal cooling. *Journal of Geophysical Research: Planets*, 112(E2).
- Parnell, J., Taylor, C. W., Thackrey, S., Osinski, G. R., & Lee, P. (2010). Permeability data for impact breccias imply focussed hydrothermal fluid flow. *Journal of Geochemical Exploration*, 106(1-3), 171-175.
- Peters, G. H., Carey, E. M., Anderson, R. C., Abbey, W. J., Kinnett, R., Watkins, J. A., ... & Beegle, L. W. (2018). Uniaxial compressive strengths of rocks drilled at Gale Crater, Mars. *Geophysical Research Letters*, 45(1), 108-116.
- Phillips, R. J., Raubertas, R. F., Arvidson, R. E., Sarkar, I. C., Herrick, R. R., Izenberg, N., & Grimm, R. E. (1992). Impact craters and Venus resurfacing history. *Journal of Geophysical Research: Planets*, 97(E10), 15923-15948.
- Pohl, J., Stöffler, D., Gall, H. V., & Ernstson, K. (1977). The Ries impact crater. In *Impact and explosion cratering: Planetary and terrestrial implications* (pp. 343-404).
- Pola, A., Crosta, G., Fusi, N., Barberini, V., & Norini, G. (2012). Influence of alteration on physical properties of volcanic rocks. *Tectonophysics*, 566, 67-86.
- Potter, R. W. K., Kring, D. A., Collins, G. S., Kiefer, W. S., & McGovern, P. J. (2012). Estimating transient crater size using the crustal annular bulge: Insights from numerical modeling of lunar basin-scale impacts. *Geophysical Research Letters*, 39(18).
- Rathbun, J. A., & Squyres, S. W. (2002). Hydrothermal systems associated with Martian impact craters. *Icarus*, 157(2), 362-372.
- Robbins, S. J., & Hynek, B. M. (2012). A new global database of Mars impact craters ≥ 1 km: 1. Database creation, properties, and parameters. *Journal of Geophysical Research: Planets*, 117(E5).
- Robbins, S. J., Singer, K. N., Bray, V. J., Schenk, P., Lauer, T. R., Weaver, H. A., ... & White, O. L. (2017). Craters of the Pluto-Charon system. *Icarus*, 287, 187-206.
- Rocholl, A., Böhme, M., Gilg, H. A., Pohl, J., Schaltegger, U., & Wijbrans, J. (2018). Comment on "A high-precision $^{40}\text{Ar}/^{39}\text{Ar}$ age for the Nördlinger Ries impact crater, Germany, and implications for the accurate dating of terrestrial impact events" by Schmieder et al. (*Geochimica et Cosmochimica Acta* 220 (2018) 146–157). *Geochimica et Cosmochimica Acta*, 238, 599-601.
- Rocscience Inc. (2017) <https://www.rocscience.com>.
- Sammis, C. G., & Ashby, M. F. (1986). The failure of brittle porous solids under compressive stress states. *Acta Metallurgica*, 34(3), 511-526.

- Sanford, W. E. (2005). A simulation of the hydrothermal response to the Chesapeake Bay bolide impact. *Geofluids*, 5(3), 185-201.
- Sapers, H. M., Osinski, G. R., Flemming, R. L., Buitenhuis, E., Banerjee, N. R., Tornabene, L. L., ... & Hainge, J. (2017). Evidence for a spatially extensive hydrothermal system at the Ries impact structure, Germany. *Meteoritics & Planetary Science*, 52(2), 351-371.
- Schaefer, L. N., Kendrick, J. E., Oommen, T., Lavallée, Y., & Chigna, G. (2015). Geomechanical rock properties of a basaltic volcano. *Frontiers in Earth Science*, 3, 29.
- Schmitt, R. T., Lapke, C., Lingemann, C. M., Siebenschock, M., & Stöffler D. (2005) Distribution and origin of diamonds in the Ries crater, Germany. in Kenkmann, T., Hörzt, F., & Deutsch, A., eds, Large Meteorite Impacts. Geological Society of America Special Paper 384, Boulder, 299-314.
- Schultz, R. A. (1993). Brittle strength of basaltic rock masses with applications to Venus. *Journal of Geophysical Research: Planets*, 98(E6), 10883-10895.
- Schultz, R. A. (1995). Limits on strength and deformation properties of jointed basaltic rock masses. *Rock Mechanics and Rock Engineering*, 28(1), 1-15.
- Schultz, R. A. (2002). Stability of rock slopes in Valles Marineris, Mars. *Geophysical Research Letters*, 29(19), 38-1.
- Shoemaker, E. M., & Chao, E. C. (1961). New evidence for the impact origin of the Ries Basin, Bavaria, Germany. *Journal of Geophysical Research*, 66(10), 3371-3378.
- Stähle, V. (1972). Impact glasses from the suevite of the Nördlinger Ries. *Earth and Planetary Science Letters*, 17(1), 275-293.
- Stähle, V., Altherr, R., Koch, M., & Nasdala, L. (2008). Shock-induced growth and metastability of stishovite and coesite in lithic clasts from suevite of the Ries impact crater (Germany). *Contributions to Mineralogy and Petrology*, 155(4), 457-472.
- Stanchits, S., Fortin, J., Gueguen, Y., & Dresen, G. (2009). Initiation and propagation of compaction bands in dry and wet Bentheim sandstone. *Pure and Applied Geophysics*, 166(5-7), 843-868.
- Stepinski, T. F., Mendenhall, M. P., & Bue, B. D. (2009). Machine cataloging of impact craters on Mars. *Icarus*, 203(1), 77-87.
- Stöffler, D. (1966). Zones of impact metamorphism in the crystalline rocks of the Nördlinger Ries crater. *Contributions to Mineralogy and Petrology*, 12(1), 15-24.
- Stöffler, D., & Grieve, R. A. F. (2007). Impactites. *Metamorphic rocks: A classification and glossary of terms, recommendations of the International Union of Geological Sciences*, 82-92.
- Stöffler, D., Artemieva, N. A., Wünnemann, K., Reimold, W. U., Jacob, J., Hansen, B. K., & Summerson, I. A. (2013). Ries crater and suevite revisited—Observations and modeling Part I: Observations. *Meteoritics & Planetary Science*, 48(4), 515-589.
- Stöffler, D., Hamann, C., & Metzler, K. (2018). Shock metamorphism of planetary silicate rocks and sediments: Proposal for an updated classification system. *Meteoritics & Planetary Science*, 53(1), 5-49.
- Sturm, S., Wulf, G., Jung, D., & Kenkmann, T. (2013). The Ries impact, a double-layer rampart crater on Earth. *Geology*, 41(5), 531-534.
- Tanaka, K. L., Skinner Jr, J. A., Dohm, J. M., Irwin III, R. P., Kolb, E. J., Fortezzo, C. M., ... & Hare, T. M. (2014). Geologic Map of Mars, US Geol. Surv. Sci. Invest. Map, 3292.
- Thomson, B. J., Bridges, N. T., Cohen, J., Hurowitz, J. A., Lennon, A., Paulsen, G., & Zacny, K. (2013). Estimating rock compressive strength from Rock Abrasion Tool (RAT) grinds. *Journal of Geophysical Research: Planets*, 118(6), 1233-1244.
- Torquato, S. (2013) Random heterogeneous materials: Microstructure and macroscopic properties. Springer Science & Business Media.
- Travis, B. J., Rosenberg, N. D., & Cuzzi, J. N. (2003). On the role of widespread subsurface convection in bringing liquid water close to Mars' surface. *Journal of Geophysical Research: Planets*, 108(E4).
- Vajdova, V., Baud, P., Wu, L., & Wong, T. F. (2012). Micromechanics of inelastic compaction in two allochemical limestones. *Journal of Structural Geology*, 43, 100-117.
- Versh, E., Kirsimäe, K., & Jõelet, A. (2006). Development of potential ecological niches in impact-induced hydrothermal systems: The small-to-medium size impacts. *Planetary and Space Science*, 54(15), 1567-1574.
- Viles, H., Ehlmann, B., Wilson, C. F., Cebula, T., Page, M., & Bourke, M. (2010). Simulating weathering of basalt on Mars and Earth by thermal cycling. *Geophysical Research Letters*, 37(18).
- von Engelhardt, W. (1990). Distribution, petrography and shock metamorphism of the ejecta of the Ries crater in Germany—A review. *Tectonophysics*, 171(1-4), 259-273.

- von Engelhardt, W., Arndt, J., Fecker, B., & Pankau, H. G. (1995). Suevite breccia from the Ries crater, Germany: Origin, cooling history and devitrification of impact glasses. *Meteoritics*, 30(3), 279-293.
- von Engelhardt, W. (1997). Suevite breccia of the Ries impact crater, Germany: Petrography, chemistry and shock metamorphism of crystalline rock clasts. *Meteoritics & Planetary Science*, 32(4), 545-554.
- Wadsworth, F. B., Vasseur, J., Scheu, B., Kendrick, J. E., Lavallée, Y., & Dingwell, D. B. (2016). Universal scaling of fluid permeability during volcanic welding and sediment diagenesis. *Geology*, 44(3), 219-222.
- Whitten, J. L., Head, J. W., Denevi, B. W., & Solomon, S. C. (2014). Intercrater plains on Mercury: Insights into unit definition, characterization, and origin from MESSENGER datasets. *Icarus*, 241, 97-113.
- Wieczorek, M. A., Neumann, G. A., Nimmo, F., Kiefer, W. S., Taylor, G. J., Melosh, H. J., ... & Konopliv, A. S. (2013). The crust of the Moon as seen by GRAIL. *Science*, 339(6120), 671-675.
- Wong, T.-f., & Baud, P. (2012). The brittle-ductile transition in porous rock: A review. *Journal of Structural Geology*, 44, 25-53.
- Wood, C. A., Lorenz, R., Kirk, R., Lopes, R., Mitchell, K., Stofan, E., & Cassini RADAR Team. (2010). Impact craters on Titan. *Icarus*, 206(1), 334-344.
- Wünnemann, K., & Ivanov, B. A. (2003). Numerical modelling of the impact crater depth–diameter dependence in an acoustically fluidized target. *Planetary and Space Science*, 51(13), 831-845.
- Wünnemann, K., Morgan, J. V., & Jödicke, H. (2005). Is Ries crater typical for its size? An analysis based upon old and new geophysical data and numerical modeling. In *Large meteorite impacts III* (Vol. 384, pp. 67-84). Boulder, Colorado: Geological Society of America.
- Wyering, L. D., Villeneuve, M. C., Wallis, I. C., Siratovich, P. A., Kennedy, B. M., Gravley, D. M., & Cant, J. L. (2014). Mechanical and physical properties of hydrothermally altered rocks, Taupo Volcanic Zone, New Zealand. *Journal of Volcanology and Geothermal Research*, 288, 76-93.
- Zhang, J., Wong, T. F., & Davis, D. M. (1990). Micromechanics of pressure-induced grain crushing in porous rocks. *Journal of Geophysical Research: Solid Earth*, 95(B1), 341-352.
- Zhu, W., Baud, P., & Wong, T. F. (2010). Micromechanics of cataclastic pore collapse in limestone. *Journal of Geophysical Research: Solid Earth*, 115(B4).
- Zhu, W., Baud, P., Vinciguerra, S., & Wong, T. F. (2011). Micromechanics of brittle faulting and cataclastic flow in Alban Hills tuff. *Journal of Geophysical Research: Solid Earth*, 116(B6).
- Zhu, W., Baud, P., Vinciguerra, S., & Wong, T. F. (2016). Micromechanics of brittle faulting and cataclastic flow in Mount Etna basalt. *Journal of Geophysical Research: Solid Earth*, 121(6), 4268-4289.

Petrophysical properties, mechanical behaviour, and failure modes of impact melt-bearing breccia (suevite) from the Ries impact crater (Germany)

Michael J. Heap, H. Albert Gilg, Paul K. Byrne, Fabian B. Wadsworth, Thierry Reuschlé

Conflicts of interest

We declare no conflicts of interest.

Petrophysical properties, mechanical behaviour, and failure modes of impact melt-bearing breccia (suevite) from the Ries impact crater (Germany)

Michael J. Heap, H. Albert Gilg, Paul K. Byrne, Fabian B. Wadsworth, Thierry Reuschlé

Highlights

- We provide porosity, permeability, Young's modulus, and strength values for suevite.
- Triaxial experiments suggest a shallow brittle–ductile transition for suevite.
- A theoretical model for granular materials captures the permeability of suevite.
- Petrophysical properties of suevite are upscaled for use in large-scale models.
- We outline the implications of these data for impacted planetary bodies.